Validating novel boundary conditions for three-dimensional mechanics-based restoration: An extensional sandbox model example

Benjamin Chauvin, Peter Lovely, Joseph Stockmeyer, Andreas Plesch, Guillaume Caumon, John Shaw

Validating novel boundary conditions for three-dimensional mechanics-based restoration: An extensional sandbox model example

AAPG Bulletin, v. 102, no. 2, p. 245-266, doi: 10.1306/0504171620817154

Benjamin P. Chauvin[1], Peter J. Lovely[2], Joseph M. Stockmeyer[3,4], Andreas Plesch[3], Guillaume Caumon[1], and John H. Shaw[3]

[1]GeoRessources, Université de Lorraine / CNRS / CREGU, ENSG, Vandœuvre-lès-Nancy, France
[2]Chevron ETC-Integrated Exploration Research Team, Houston, TX 77002, USA
[3]Earth and Planetary Sciences, Harvard University, Cambridge, MA 02138, USA
[4]now at: Chevron North America Exploration & Production, Houston, TX 77002, USA

Abstract

Geomechanical restoration methods are dependent on boundary conditions to ensure geological consistency of the restored model in terms of geometry and strain. Classical restoration boundary conditions, such as flattening a datum horizon, may lead to inconsistent displacement and strain fields.

We restore a laboratory structural sandbox model with known deformation history in order to develop guidelines for definition of boundary conditions that produce improved results from geomechanical restorations. The sandbox model has a basal silicone layer, includes syn-kinematic deposition, and is characterized by structures analogous to those found in supra-salt extensional environments. The deformed geometry is interpreted from 3D tomography imaging, and a time-series of cross-section tomography images provides a benchmark to quantify restoration error and inform boundary conditions.

We confirm that imposing a lateral displacement equal and opposite to far-field tectonic shortening or extension provides a more accurate restoration. However, the amount of displacement may not be known in real cases. We therefore test several established methods, using only the unrestored geometries, to assess the amount of shortening that should be used to guide geomechanical restorations. An accurate estimation is provided by the area-depth method and potentially by a dilatation analysis. Additionally, novel fault compliance boundary conditions produce improved results in the vicinity of crossing and branching faults. Application of similar methods should produce improved restoration of natural geologic structures.

Introduction

Structural restoration is a valuable tool to investigate the geometries of geological structures through time, assess the validity of structural interpretations, and analyze strain fields (e.g., Chamberlin, 1910; Dahlstrom, 1969; Gratier et al., 1991; Léger et al., 1997; Williams et al., 1997; Rouby et al., 2002; Griffiths et al., 2002; Dunbar and Cook, 2003; Muron, 2005; Groshong, 2006; Maerten and Maerten, 2006; Moretti, 2008; Durand-Riard et al., 2010, 2013b; Maerten and Maerten, 2015; Vidal-Royo et al., 2015; Stockmeyer et al., 2017). Over more than fifteen years, geomechanical restoration approaches that approximate natural rock behavior have been developed to overcome several limitations of traditional geometrical restoration methods (e.g., Fletcher and Pollard, 1999; Maerten and Maerten, 2001; Santi et al., 2003; Muron, 2005; Moretti et al., 2006; Maerten

and Maerten, 2006; Moretti, 2008; Guzofski et al., 2009; Durand-Riard et al., 2010; Lovely et al., 2012; Vidal-Royo et al., 2012; Durand-Riard et al., 2013b; Maerten and Maerten, 2015; Vidal-Royo et al., 2015; Tang et al., 2016). Mechanics-based restoration follows the fundamental physical laws of continuum mechanics, i.e., mass and linear momentum conservations, and invokes a linear or non-linear elastic constitutive relation to govern rock deformation. Boundary conditions are required to unfault and unfold geological structures simultaneously in the simplest manner possible and to obtain a unique solution. Three general types of boundary conditions have been shown to yield geologically reasonable results: (1) an imposed displacement to flatten the uppermost horizon, (2) a set of contacts to ensure fault compliance (neither gap nor penetration between fault blocks, and contact of the uppermost horizon fault cutoff lines), and (3) the definition of pin walls, pin lines and pin nodes to fix degrees of freedom and guarantee that the solution is unique (e.g., Plesch et al., 2007; Guzofski et al., 2009; Vidal-Royo et al., 2012; Durand-Riard et al., 2013a,b; Stockmeyer et al., 2017).

Boundary conditions have an important impact on the restored geometry. While several studies have shown that simple boundary conditions can yield viable restoration results (e.g., Maerten and Maerten, 2006; Guzofski et al., 2009), there are many pitfalls. For example, Lovely et al. (2012) show a simple example in which classical boundary conditions applied to a geomechanical restoration lead to unphysical strain fields and that a different set of boundary conditions significantly changes the resultant strain field (see Figure 1 in Lovely et al. (2012)). This uncertainty in appropriate boundary conditions is particularly problematic if one intends to analyze the corresponding stress or strain for fracture analysis or other purposes (Maerten and Maerten, 2006; Mejía-Herrera et al., 2014; Stockmeyer et al., 2017). The problems illustrated by Lovely et al. (2012) are: (1) there may be instances when the classical boundary conditions, as defined above, may be unphysical and (2) there is no specific guideline to choose appropriate boundary conditions in restoration. Durand-Riard (2010); Lovely et al. (2012) and Durand-Riard et al. (2013b) suggest that these classical boundary conditions may be insufficient to restore geologically consistent and physical strain. They show on synthetic models that a lateral displacement boundary condition along a boundary wall is necessary to recover the expected strain in compressive, extensional, and strike-slip and oblique-slip contexts. In addition, they show that the restoration displacement field is only consistent with the forward displacement field when the amount of the displacement condition on a wall is equal to the amount of forward displacement. These works highlight the need for additional constraints derived from geologic or tectonic insights for mechanics-based restoration. The main challenge for defining these additional constraints is that they require knowledge of the deformation history, which is rarely accessible and, ideally, should be an output of the mechanics-based restoration. Moreover, these studies of boundary conditions were applied to numerical or synthetic models, which are typically idealizations of natural geologic structures, and present additional uncertainties and assumptions (structural interpretation, deformation path, etc.).

Models from laboratories are often used to validate restoration methods (e.g., Schultz-Ela, 1992; Yamada and McClay, 2003; Maerten and Maerten, 2006; Groshong et al., 2012; Moretti and Callot, 2012). As they are laboratory experiments, the forward boundary conditions and the mechanical behaviors are known, and the kinematic evolution of structures may be recorded. Moreover, the interpretation uncertainties of these deformed forward models are generally small, such that the applied boundary conditions can be considered the primary source of uncertainty in restoration attempts. This is a significant benefit compared to restoration attempts of natural structures, where restoration uncertainties result from the interplay of boundary condition uncertainties and of structural interpretation uncertainties (Gratier et al., 1991; Schultz-Ela, 1992).

In this study, we performed a sequential restoration on an analog model deformed in laboratory. Computed tomography (CT) images capture the sequential development of this analog model. These images constrain the forward deformation path of each structure, capturing paleo-geometries through time on one edge of the analog model, and, thus, provide a reasonable benchmark for restoration quality and boundary condition testing. In the following, we describe the structural sandbox model and our tests of boundary conditions with the goal of restoring deformed geometries and related fault slip that are consistent with the reference model paleo-geometries. New fault compliance boundary conditions are proposed to handle the complex fault network identified on the CT images. In addition, we propose methods to define lateral displacement boundary conditions without detailed knowledge of the forward deformation path, improving the viability of the 3D geomechanical restoration method for use with natural geologic structures.

1 Case study and its representativeness

1.1 Extensional sandbox model: supra-salt structures

Geologists typically have access only to the present-day state of deformed strata, often times informed by sparse and uncertain data. Such data may be consistent with multiple interpretations that may vary significantly (e.g., Frodeman, 1995; Bond et al., 2007; Wellmann et al., 2010; Bond, 2015; Cherpeau and Caumon, 2015). Thus, the analysis of rock deformation through time is made difficult by the lack of direct information on paleo-structures and the limitations of the available data. To overcome some of these concerns, laboratory analog models are widely used to model viable deformation styles and paths of natural geologic structures (e.g., McClay, 1990). They provide a way to follow the evolution of well-known geometries under known physical mechanisms through time. X-ray tomography is a common, non-destructive method to image the 3D structures of a deformed structural sandbox (e.g., Colletta et al., 1991; Callot et al., 2012). X-ray tomography resolution on an analog model is generally sufficient to study deformed structures with minimal geometric uncertainties. Distinct horizons and faults can be observed due to density contrasts in the model's stratigraphy. Thus, as pointed by Colletta et al. (1991), X-ray tomography is a valuable tool to analyze the temporal evolution of laboratory models. Moreover, an analog model must be properly defined to reproduce the behavior of geological structures. Scale, mechanical materials, physical processes, and timing are examples of parameters to consider for the purpose of assessing the degree to which analog models represent natural structures.

In this paper, we restore a laboratory model analogous to supra-salt extensional structures observed in salt basins around the world, such as the Gulf of Mexico, Angola and Morocco. It is well established that dry sand (no cohesion) is a viable material for modeling brittle and ductile rock deformation in sedimentary systems (e.g., Panien et al., 2006; Victor and Moretti, 2006; Dooley et al., 2007; Callot et al., 2012; Moretti and Callot, 2012; Darnault et al., 2016). Moreover, Weijermars et al. (1993); Victor and Moretti (2006) and Moretti and Callot (2012), among others, have shown that an analog composed by a stack of sand above silicone can produce structures representative of natural salt basins. Silicone has a very weak rheology relative to sand. Thus, sand layers deform and may penetrate into the silicone. This effectively reproduces the subsurface at the interface between a viscous salt layer and overlying brittle rocks (Weijermars et al., 1993).

Our work is based on a deformed structural sandbox done in laboratory by IFPEN (`http://www.ifpenergiesnouvelles.fr`) and C&C Reservoirs, 2016, DAKS^{TM} - Digital Analogs Knowledge System (`http://www.ccreservoirs.com`) (Figure 1) to reproduce extensional salt structures. The model box was initially composed of two horizontal layers composing a pregrowth stratigraphy: one of silicone at the bottom with a thickness of 1.8 cm (0.71 in), and one of sand above with a thickness of 4 mm (0.2 in). The initial thickness (along Z direction) of the pregrowth strata is 2.2 cm (0.87 in). Along the Y axis the structural sandbox length is 10 cm (3.9 in), and 18 cm (7.1 in) along the X axis. The model box was inclined by 1.5° (Weijermars et al., 1993; Victor and Moretti, 2006). Deformation was induced initially by gravity sliding along this tilt (toward the eastern side on Figure 1). On the down-dip end of the model there was no wall to restrain the motion of the materials. As the model deformed, alternating layers of pyrex or sand were deposited (one layer every 16 min in mean), further driving deformation by a combination of gravity spreading and gravity gliding (Victor and Moretti, 2006). This deposition of successive stratigraphic horizons during deformation represents syn-tectonic strata (i.e., growth strata). As pyrex and sand strata are deposited above the silicone, this experiment describes supra-salt structures. At each depositional time step, the newly deposited sediments filled the available model space. In total, 12 layers were deposited (Figure 1) over the course of the forward analog model. The total duration of the experiment is 4h16min. The properties of the silicone, pyrex and sand are provided in Table 1. The scaling from the analog model scale to real field scale is approximately 1 cm (0.4 in) for 1 km (0.6 mi), consistently with similar analog models (Ellis and McClay, 1988; Dooley et al., 2007; Wu et al., 2009; Hidayah, 2010; Darnault et al., 2016). See Hubbert (1937) and Ramberg (1981) for more details about the methods used to define this scaling. It is possible to distinguish silicone, sand, pyrex and the fault offsets by tomographic imaging due to their density contrasts. Indeed, faults are visible in the analog model due to sand and pyrex dilatation (areas of lower density) (Colletta et al., 1991; Cobbold and Castro, 1999; Le Guerroué and Cobbold, 2006; Groshong et al., 2012). Moreover, sand and pyrex have a sufficient Hounsfield density contrast (Table 1) to distinguish them in X-ray tomography (Panien et al., 2006; Darnault et al., 2016), allowing the analysis of fault offset. In addition, we assume that friction is negligible on the edges of the structural sandbox model (Souloumiac et al., 2012).

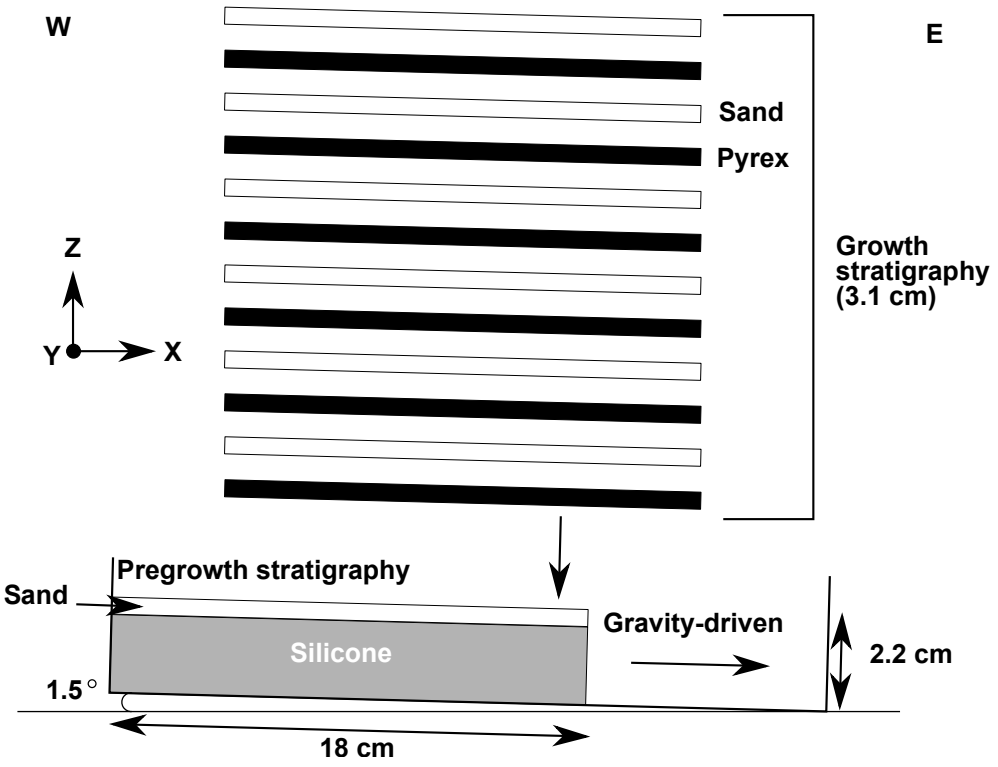

Figure 1: An initial pregrowth stratigraphy composed by a layer of silicone and a layer of sand is deformed by gravity. The initial dimensions of the structural sandbox are: 18 cm (7 in) along X axis, 10 cm (4 in) along Y axis, and 2.2 cm (0.9 in) along Z axis. At each time step, a layer of sand or pyrex is deposed to generate syn-sedimentary deformations. Twelve layers are deposed forming a growth stratigraphy (3.1 cm, 1.2 in). Figure created from C&C Reservoirs, 2016, DAKS^{TM} - Digital Analogs Knowledge System and IFPEN documentation.

	Rheological behavior	Relative density	Grain size (μm)	Internal friction angle (°)	Cohesion (μPa)	Viscosity (mPa.s or cps)	Hounsfield density (HU)
Sand	Brittle	1.3-1.5	100 (0.004 in)	40	1-2 (10^{-10} - 2×10^{-10} psi)		500
Pyrex	Brittle	1.2	100 (0.004 in)	32-36	> 5 (5×10^{-10} psi)		150
Silicon SGM36	Ductile	0.97				5.10^7	95

Table 1: The relative density (unitless) of a material corresponds to the density of this material divided by the density of water. The Hounsfield density (in HU, no SI equivalence) is a measure of the X-ray attenuation in a medium. Data from C&C Reservoirs, 2016, DAKS^{TM} - Digital Analogs Knowledge System and IFPEN documentation.

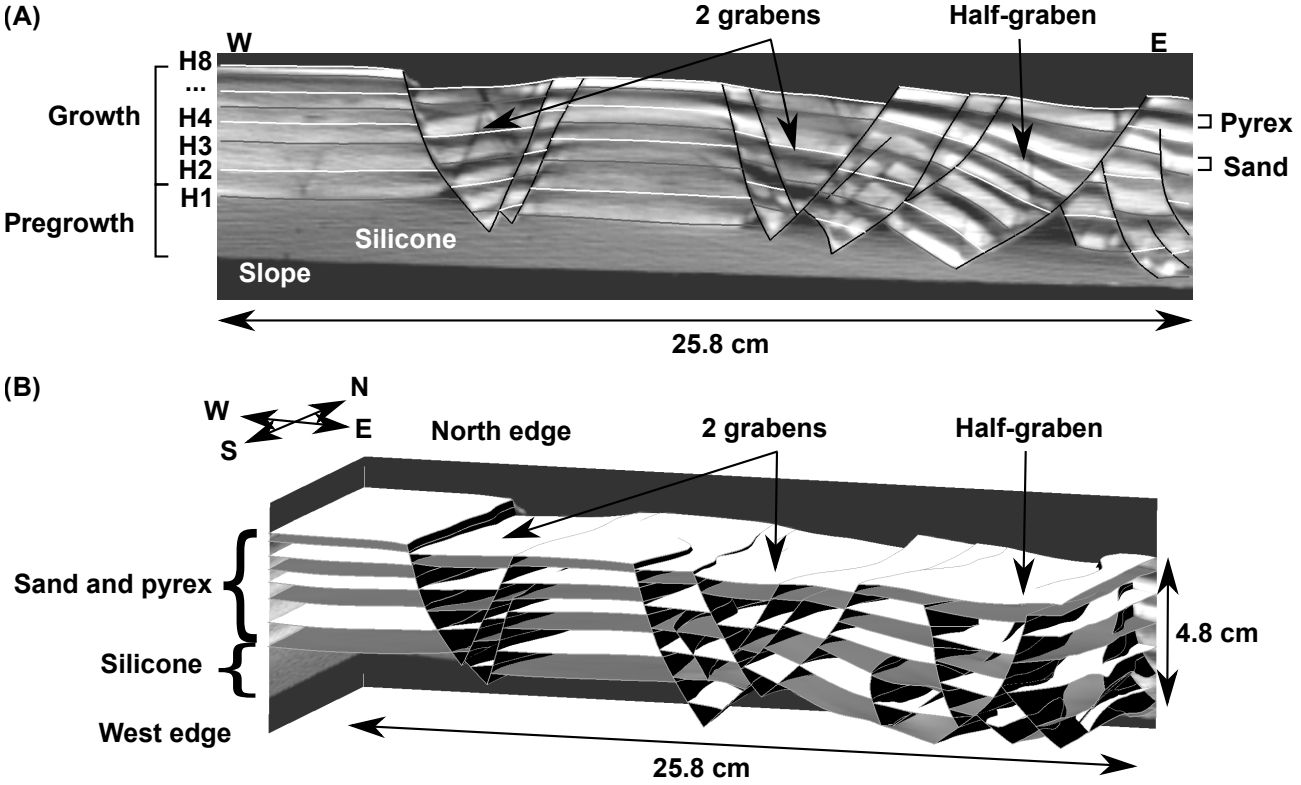

Figure 2: (A) Interpretation of the north CT image at the final stage of the structural sandbox experiment. The uppermost layer is a layer of sand, the others are composed by a layer of pyrex and a layer of sand. (B) Structural model of the extensional analog model. It is formed by 8 horizons (white and gray surfaces) and 22 normal faults (black surfaces). CT images of the northern and the western edges are displayed. CT data courtesy of IFPEN and C&C Reservoirs, 2016, DAKS^{TM} - Digital Analogs Knowledge System.

1.2 Interpretation of the structural sandbox model

A 3D X-ray tomography volume of the final state of the deformed box was produced. The volume is defined by an X-ray tomography section every 3 mm (0.1 in) along the Y axis, and an X-ray tomography section every 0.6 mm (0.02 in) along the X and Z axes, producing a tomography volume that can be interpreted with similar methods as a 3D seismic reflection survey (Figure 2A). Unfortunately, we had access to only a part of the structural sandbox volume. Indeed CT imaging only recorded through time a specific interval of the structural sandbox. Beyond this interval, down-dip, the analog model continued to deform but was out of the scope of the CT imaging. Although we analyzed the majority of the volume, a part on the eastern side could not be considered in our study. From our interpretation, we built a 3D explicit numerical structural model (boundary representation, Figure 2B) using SKUA-GOCAD (Paradigm, 2015), in which horizon and fault surfaces are conformal (Caumon et al., 2004). The geological model is composed of three primary structures: two grabens in the western and central regions of the model, and a series of west-dipping half-grabens in the eastern region of the model. The layer of silicone representing autochthonous salt is not explicitly represented in our numerical model. Within the analog model, we identified 52 faults. As the purpose of the modeling is the restoration and the strain analysis, faults with small offsets were ignored for simplicity (Figure 3B). Additionally, a few faults that define narrow fault blocks were removed and the horizons were made continuous (Figure 3C). As discussed by Vidal-Royo et al. (2012) and Pellerin et al. (2014), this eases the meshing and avoids numerous small volumetric elements in the 3D mesh used in restoration, which reduces the computational time of restorations. The final numerical model is composed of 8 horizons and 22 normal faults. The uppermost layer in the structural model corresponds to the uppermost layer of sand in the experiment. Below, each layer in the model represents a layer of pyrex and the underlying layer of sand. The six pyrex basal horizons were not modeled for simplicity. Figure 2A presents the model stratigraphy on the north CT image.

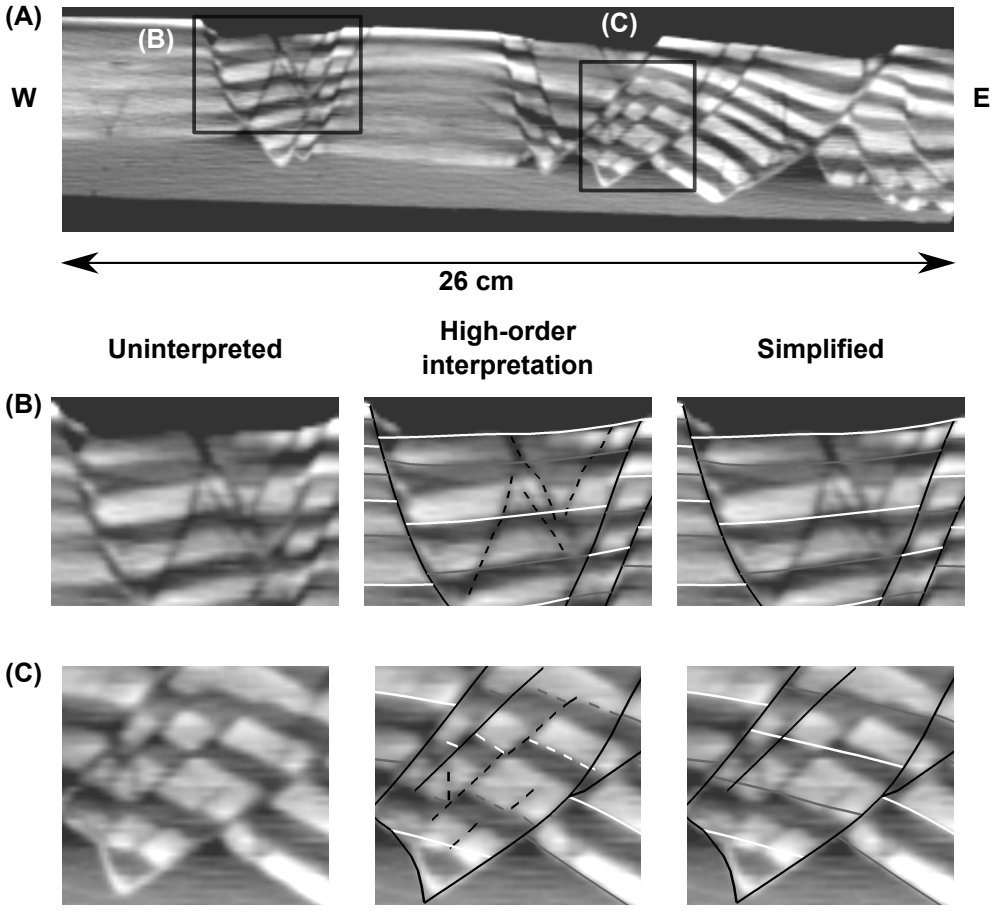

Figure 3: Two examples of interpretation and simplification on the northern edge of the 3D tomography (interpreted as a seismic cube). (A) North CT image at the final stage of the structural sandbox experiment. Each example is in black square. (B)-(C) Interpretation examples composed from the left to the right by: the uninterpreted CT image part, its high order interpretation, and its simplification. The simplified interpretation is the one used for the restorations. Dashed lines are the interpreted elements not kept in the final model. Continuous lines are the interpreted elements kept in the final model. Faults are in black. Horizons are in white or gray. (B) Interpretation and simplifications on a part of the western graben. (C) Several faults delimiting relatively small fault blocks were neglected to facilitate 3D mesh generation. Horizons were made continuous, introducing local mismatches with the data. CT data courtesy of IFPEN and C&C Reservoirs, 2016, DAKS^{TM} - Digital Analogs Knowledge System.

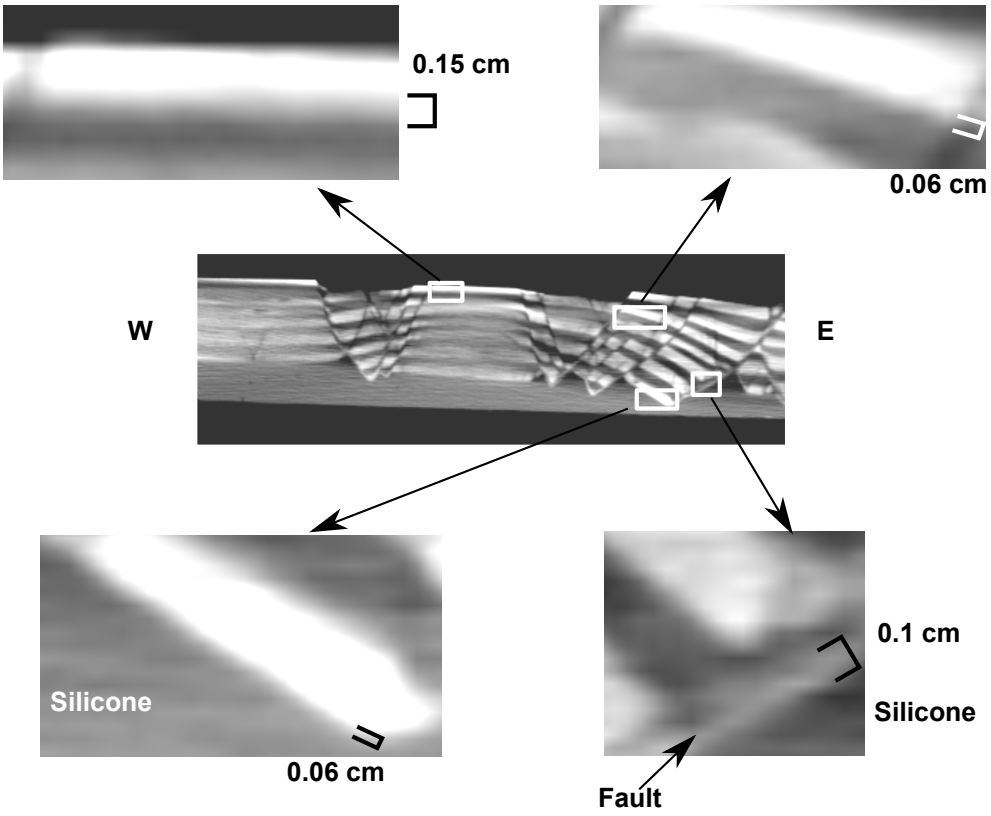

Figure 4: Four examples of the north CT image at the final stage of the structural sandbox experiment are displayed with the approximated uncertainty areas (gray zones between white and black layers). The picking imprecision is on average of 0.1 cm. CT data courtesy of IFPEN and C&C Reservoirs, 2016, DAKS^{TM} - Digital Analogs Knowledge System.

1.3 Structural uncertainties

Although the analog structures are well imaged, uncertainties in our structural interpretations exist. This is largely the result of approximating diffuse horizons and faults in the analog model with discrete surfaces in our structural representation. Thus, quantifying our interpretation precision is necessary in order to properly evaluate the quality of subsequent restoration results. Figure 4 illustrates four examples of interpretation uncertainties of the deformed analog model. Boundaries between white layers (sand) and black layers (pyrex or silicone) are typically blurred gray (Figure 4). The thickness of these gray transition zones provides an estimate of the uncertainty associated with an interpreted horizon between two strata intervals. Although this thickness may vary laterally (Figure 4), we estimate an error of 0.1 cm (0.04 in) is a representative uncertainty for all of our interpretations. We will be mindful of this precision as we analyze our restoration results. We also note that other restoration uncertainties, such as finite element approximation or mechanical simplifications, although present, are not considered in our uncertainty analysis.

2 Restoration settings

2.1 Physical volumetric model

We created a 3D mesh (Figure 5A) from the structural model (Figure 2B) using the Geogram (Lévy, 2015), RINGMesh (Botella et al., 2016; Pellerin et al., 2017), VorteXLib (Botella, 2016a,b) and TetGen (Si, 2015a,b) libraries. It is composed of 647,558 tetrahedra and the average tetrahedron length is 0.25 cm (0.098 in). We made some efforts to reduce the number of tetrahedra, which impacts the restoration computational time, and to avoid imprecision due to a coarse mesh. The VorteXLib library enabled us to develop a 3D mesh maximizing the quality of the tetrahedra (equilaterality) to avoid numerical issues during restorations (Parthasarathy et al., 1994; Shewchuk, 2002; Munson, 2007). The silicone layer was not represented in the model used for the restoration for two primary reasons. First, its rheology is far weaker than the sand and the pyrex, and thus is not considered to contribute any significant resistance. Second, the viscous behavior of the silicone interval cannot be properly

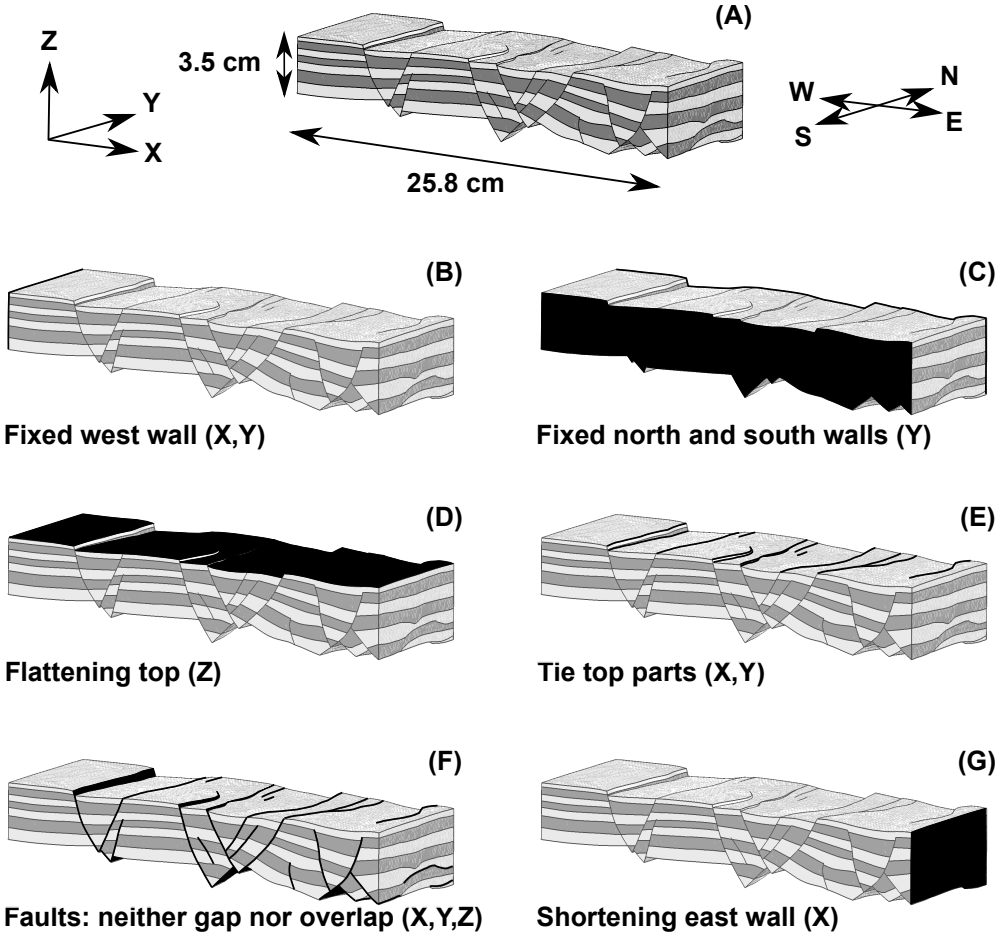

Figure 5: (A) Volumetric model at the final stage of the structural sandbox experiment. The presented boundary conditions are applied on this model. Equivalent conditions are assigned to restore the other horizons (sequential restoration). (B) Western wall: no motion is allowed along X and Y directions. (C) Northern and southern walls: no motion is allowed along Y direction. (D) Uppermost horizon: flattening. This condition explicitly constrains Z component of mesh nodes. (E) Uppermost horizon parts are tied. It is a fault contact condition. For each fault cutting the uppermost horizon, the footwall cutoff line and the hanging wall cutoff line are tied together. This condition is applied on X and Y directions. Z component is ensured by the flattening, see (D). (F) For each fault, fault mirrors are tied (neither gap nor penetration). (G) Eastern wall: shortening along X direction. This condition is optional.

represented by the elastic constitutive law invoked in our restoration method. Thus, we focused on restoration of the sand and pyrex layers that overlie the silicone, with the base of the model being a free surface that represents the top of the silicone (Stockmeyer and Guzofski, 2014). As sand and pyrex are rheologically similar (Panien et al., 2006), we applied homogeneous elastic properties for the entire model: Young's modulus was set to 70 GPa (10^7 psi) and Poisson's ratio to 0.2 (Holtzman et al., 2009).

2.2 Classical boundary conditions

A video of one edge of the analog model was recorded by X-ray computed tomography, allowing us to visualize the deformation and model geometries through time. The deformation front was located on the eastern side of the model. In contrast, the western side was only weakly deformed (Figure 2A). Thus, we fixed the western wall in the X and Y directions during the restoration, allowing it to only move vertically (Figure 5B). As the experiment is inside a box, no flow occurred in the north-south direction (Y axis) through the northern and southern walls. Therefore, during the restoration, we fixed the northern and the southern walls in Y (Figure 5C), as recommended by Durand-Riard (2010) and Durand-Riard et al. (2013b) in other deformation contexts. At each restoration step, we set a datum boundary condition for the uppermost stratigraphic surface because we know the original depositional gradient (Figure 5D). As the model had a tilt of 1.5° toward east, we rotated the entire model before each restoration. This allowed us to set our datuming boundary condition to a constant Z

value (Figure 5D). We rotated our restored models to their proper geometries for proper comparisons between the numerical models and the CT images. The basal horizon, which defines the interface between sand and silicone, i.e., H1, was defined as a free surface (e.g., Stockmeyer and Guzofski, 2014).

We also defined fault contact conditions to tie the hanging wall and footwall cutoff lines of the uppermost (flattened) horizon (Figure 5E) and to avoid any gap or penetration along fault surfaces (Figure 5F). We ensured fault compliance by contact mechanics (Wriggers and Laursen, 2006) which is a master-slave approach adapted to restoration purposes by Muron (2005), and Maerten and Maerten (2006). This method enables us to tie fault blocks without any friction along fault planes (Muron, 2005; Maerten and Maerten, 2006; Wriggers and Laursen, 2006). The slave surface cannot penetrate nor have a gap with the master surface but the contrary is possible when faults are curved, owing to limited mesh resolution. No relative displacement constraint between the master and the slave is defined: motion is bilateral and is a consequence of both energy minimization and the constraint for the two sides of the fault to be in contact. In the case of the contact of the fault cutoff lines of the restored (uppermost) horizon (Figure 5E), the throw is already defined by the datuming condition applied on the Z-component of the uppermost horizon (Figure 5D). The heave is defined by contact mechanics as explained above.

2.3 Non-classical boundary condition: imposed shortening condition

As extension clearly occurred during forward deformation, we test an optional lateral shortening condition applied to the down-dip model boundary during restoration. We consider this boundary condition analogous to those suggested by Durand-Riard (2010); Lovely et al. (2012) and Durand-Riard et al. (2013b). This optional shortening condition is limited to motion along the X axis (i.e., in the west-east direction) and is applied to the eastern wall (Figure 5G). In this paper, when we refer to a "no shortening condition", we refer to a restoration scenario without this shortening condition set to the down-dip wall. In these scenarios, the eastern wall is free to move along any direction and the resultant shortening is the output of the restoration, ultimately controlled by the datum and fault slip conditions.

2.4 Non-classical boundary conditions: contacts between faults

The complexity of a model increases substantially with the numbers of faults due to the increasing number of the interactions between them and with the horizons (i.e., cutoff relationships, (Pellerin et al., 2015)). The model that we restored presents numerous connections between faults (Figures 2B and 5A): 22 faults including 5 faults cut and displaced by later faults (offset faults), no isolated fault and 27 branch lines. Proper management of such a complex fault network is a difficult task during structural modeling, but also during each step of a sequential restoration. To accomplish this task, we present in this paper two additional fault contact boundary conditions that we applied in our restorations. These conditions use contact mechanics, as classical fault contact boundary conditions that we previously defined (Wriggers and Laursen, 2006).

2.4.1 Handling branching faults

In our structural modeling procedure, a fault is represented by two surfaces, one for the hanging wall and one for the footwall. This and the fault contact conditions enable the sliding of the fault blocks along the faults (Figure 6). As a result, a branch line between two faults is represented on the main fault by two surface internal borders (black dots in (B1) and (C1) in Figure 7 with $F1^-$ the main fault). In the case of branching contacts between faults, discontinuities may occur in the restored state if care is not taken (Figure 7B). Therefore, we set contact conditions to tie the internal surface borders and thus avoid internal gaps or overlaps in the restored state (Figure 7C).

2.4.2 Handling offset fault surfaces

There were several situations where a fault surface was offset by a different fault. To properly characterize these faulted faults, we split each offset fault into two or more distinct fault surfaces. For example, Figure 8 shows that fault F1 is cut and displaced by fault F2. In this case, F1 was represented by two independent faults: F1-hw and F1-fw where the labels -hw and -fw respectively refer to the hanging wall and footwall sides of F2. As a result, F1-hw and F1-fw are able to move independently. However, as F1 was originally a single fault surface, and since we know all of the faults are normal faults at all times during the forward model, we know that the slip between F1-hw and F1-fw along F2 should decrease through the restoration until it becomes null. In other words, the distance between F1-hw and F1-fw should decrease along F2 until they merge. Upon removing of

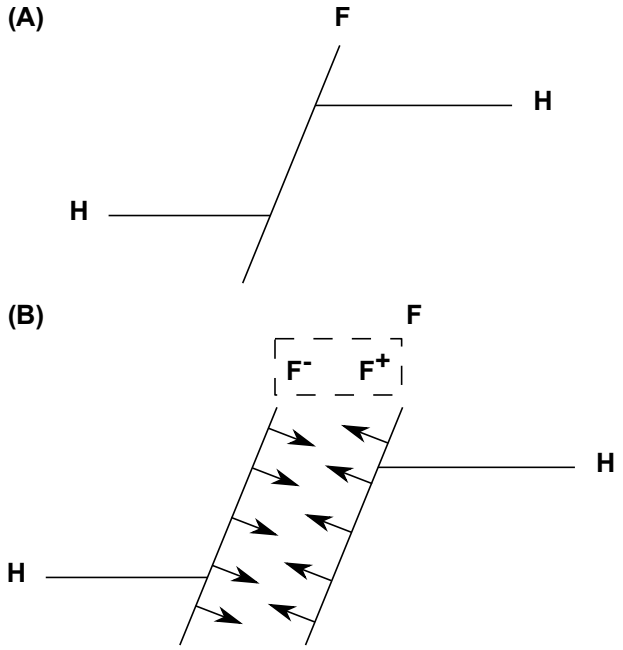

Figure 6: (A) Fault and horizon topology as in a boundary representation of a geological model. Fault F (single surface) splits a horizon H in two parts. (B) Fault and horizon topology as in a volumetric model to restore. Fault F corresponds to two surfaces, one for the hanging wall (F^-) and one for the footwall (F^+). Arrows represent fault contact boundary conditions used in restoration. These conditions tie both surfaces which compose F, allowing sliding without friction.

all the fault offsets, F1-hw and F1-fw should no longer behave independently, but form a single continuous fault surface. We ensure this condition by a set of contact conditions that aims to tie the different connected components of an offset fault (Figure 8). In our case, we were able to quickly determine which restoration steps to apply this contact condition for a particular offset fault (presenting apparent continuity) by investigating the CT images that recorded the forward deformation process.

3 Results: restoration of the analog model

3.1 Sequential restoration

We performed a partial sequential restoration using RINGMecha (Chauvin and Mazuyer, 2016), a mechanics-based restoration library based on the work of Muron (2005) and Durand-Riard (2010). We used a time-independent finite element solver to perform the restoration (e.g., Zienkiewicz and Taylor, 2000a,b; Belytschko et al., 2013) with a small deformation assumption. After each restoration step, we removed the uppermost, restored layer before performing the subsequent restoration step. Using the classical and newly defined boundary conditions described above, we performed four steps of sequential restoration for our model (Figures 9-12), yielding a restoration of more than half of the growth strata interval. Restorations with a shortening boundary condition are in Figures 9E, 10E, 11E, and 12E. As we had the CT images of the paleo-states of the northern wall, we evaluated the shortenings by following a marker on the eastern wall. The measured, incremental shortenings for each restoration step are: 1.44 cm (0.567 in), 0.71 cm (0.28 in), 1.85 cm (0.728 in) and 1.85 cm (0.728 in). Qualitatively, the general consistency on the northern edge between the restorations with prescribed shortening and the reference CT images is quite good, indicating a robust and accurate restoration. Restorations without a shortening boundary condition are shown in Figures 9F, 10F, 11F, and 12F. In these models, we only avoided the shortening boundary condition for the last restoration step. For example, the result shown in Figure 9F was not used as the starting model for the restoration in Figure 10F. The starting model for Figure 10F was generated by removing the restored, uppermost layer from the model shown in Figure 9E. In this way, we attempt to avoid propagating errors. For each restoration step that does not include the shortening boundary condition (Figures 9F, 10F, 11F, and 12F), it is clear that there was not enough extension restored to be considered an acceptable restoration result. In each case, the restored faults are too far down-dip relative to the reference position obtained from the CT tomography video. In contrast, the restorations that included the shortening boundary condition provide a better qualitative match between the restored models and the reference CT images

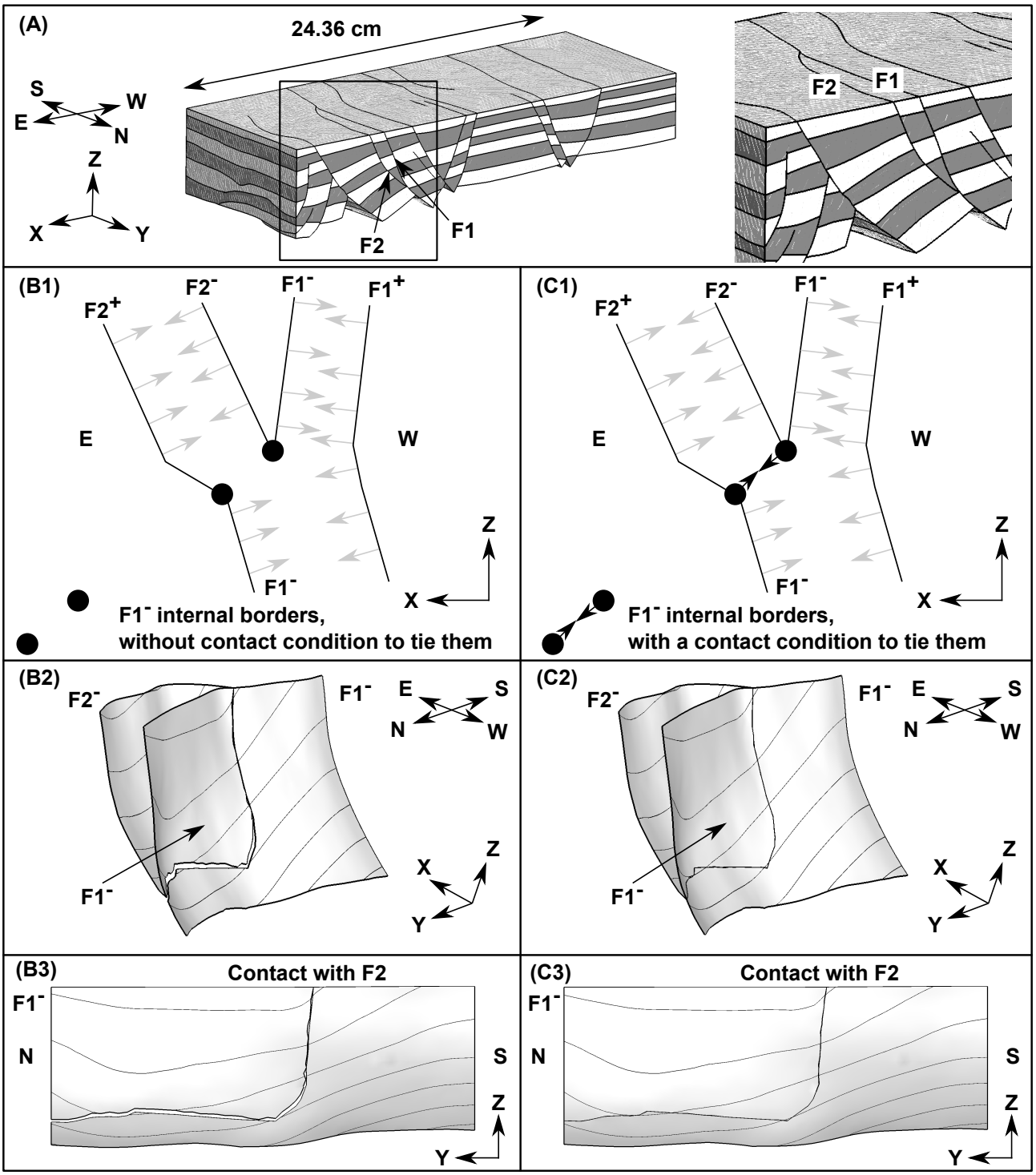

Figure 7: The subfigures have different views as indicated by the axes. (A) Restored model (first step) with an eastern shortening of 1.44 cm. The studied contact is between F1 and F2: F2 branches onto F1. (B) Contact between F1 and F2 after restoration when no contact condition (B1) is set to ensure a proper contact between these faults: there is a hole between the connected components that compose F1 (B2 and B3). (C) Contact between F1 and F2 after restoration when a contact condition (C1) is set to ensure a proper contact between these faults (black arrows). Continuity (within the contact precision scale) exists between the connected components that compose F1 (C2 and C3). In (B1) and (C1) gray arrows represent classical fault contact conditions, and in (B2), (B3), (C2) and (C3) X-coordinate contours are displayed on fault surfaces. + and - signs are an arbitrary convention to make the distinction between fault sides (see Figure 6)

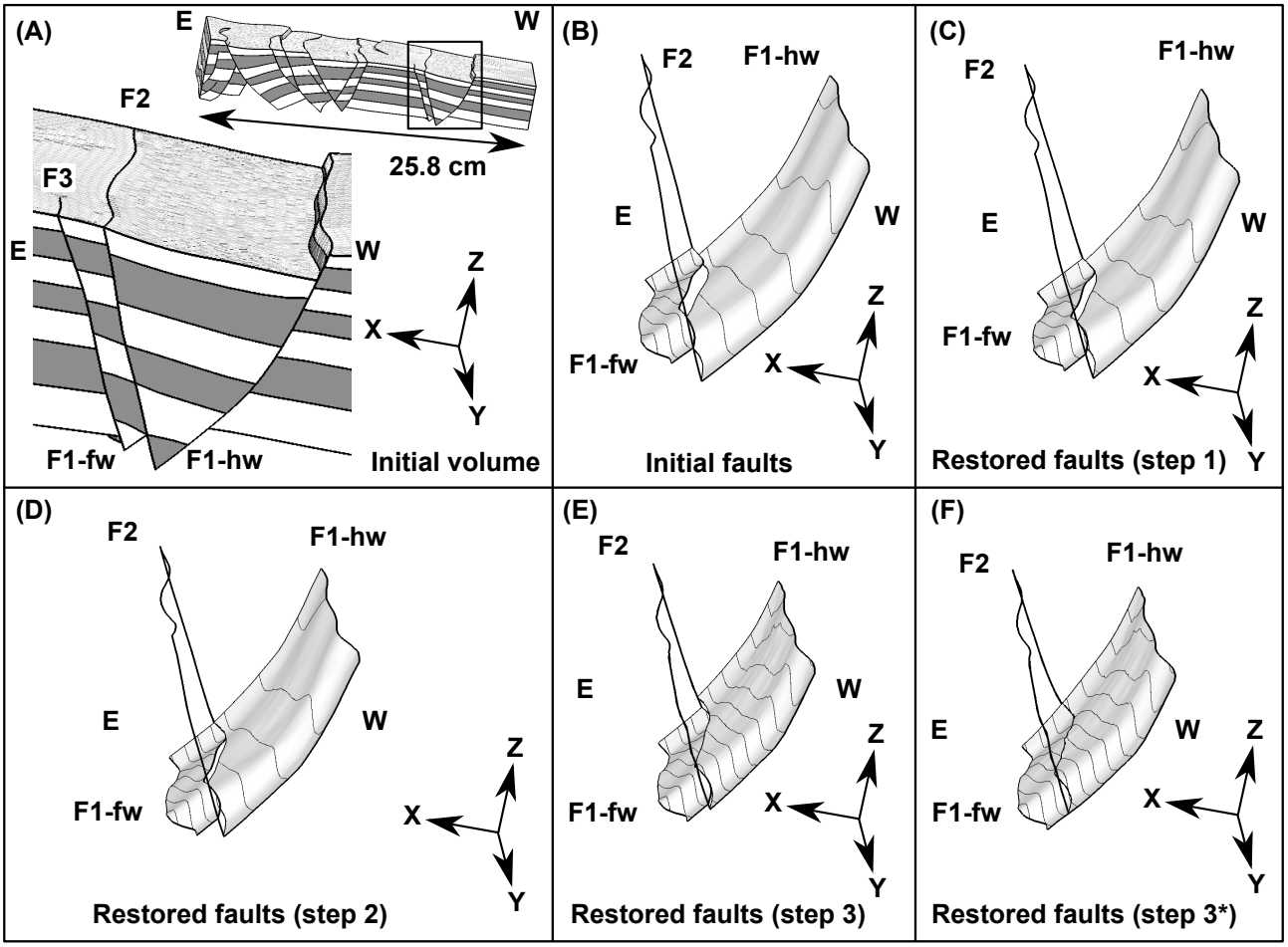

Figure 8: (A) Initial unrestored model. This example focuses on a fault F1 cut into two parts by another fault: a hanging wall part F1-hw and a footwall part F1-fw. The hanging wall and footwall definition of F1 is relative to the fault that cuts F1: F2. In all the remaining subfigures, F2 is visible by its border, and X-coordinate contours are displayed on F1 surface. (B) Initial unrestored shape of F1. It is composed of two disconnected connected components. (C) Shape of F1 after the first restoration step. F1 is still into two parts. (D) Shape of F1 after the second restoration step. Both connected components of F1 are partially connected on the southern side. (E) Shape of F1 after the third restoration step. It seems visually that F1 should be continuous. (F) Shape of F1 after the third restoration step as (E) with additional contact constraints to ensure continuity between the hanging wall and the footwall.

(Figures 9E, 10E, 11E, and 12E). For our model with the prescribed material properties, the classical boundary conditions alone are not sufficient to produce a reasonable restoration result.

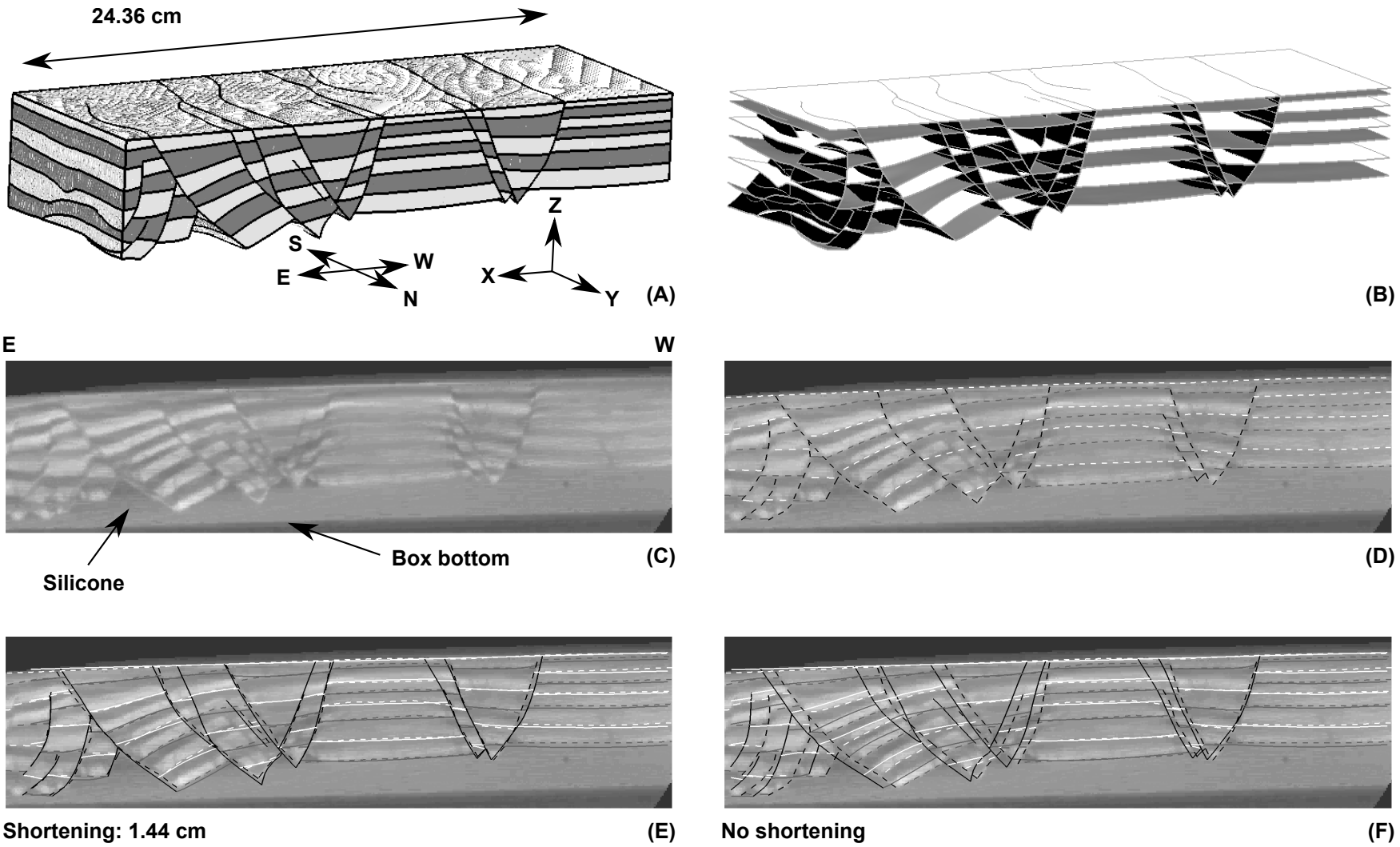

Figure 9: (A) Restored volumetric model obtained with a shortening of 1.44 cm. (B) Restored surface model obtained with a shortening of 1.44 cm. (C) Uninterpreted CT image of the northern edge at H8 deposition time. (D) Interpreted CT image of the northern edge at H8 deposition time (dashed curves). The interpretation represents the reference solution. (E) Same as (D) with the restoration result with a shortening boundary condition of 1.44 cm (continuous curves). (F) Same as (D) with the restoration result without shortening boundary condition (continuous curves). CT data courtesy of IFPEN and C&C Reservoirs, 2016, DAKS^{TM} - Digital Analogs Knowledge System.

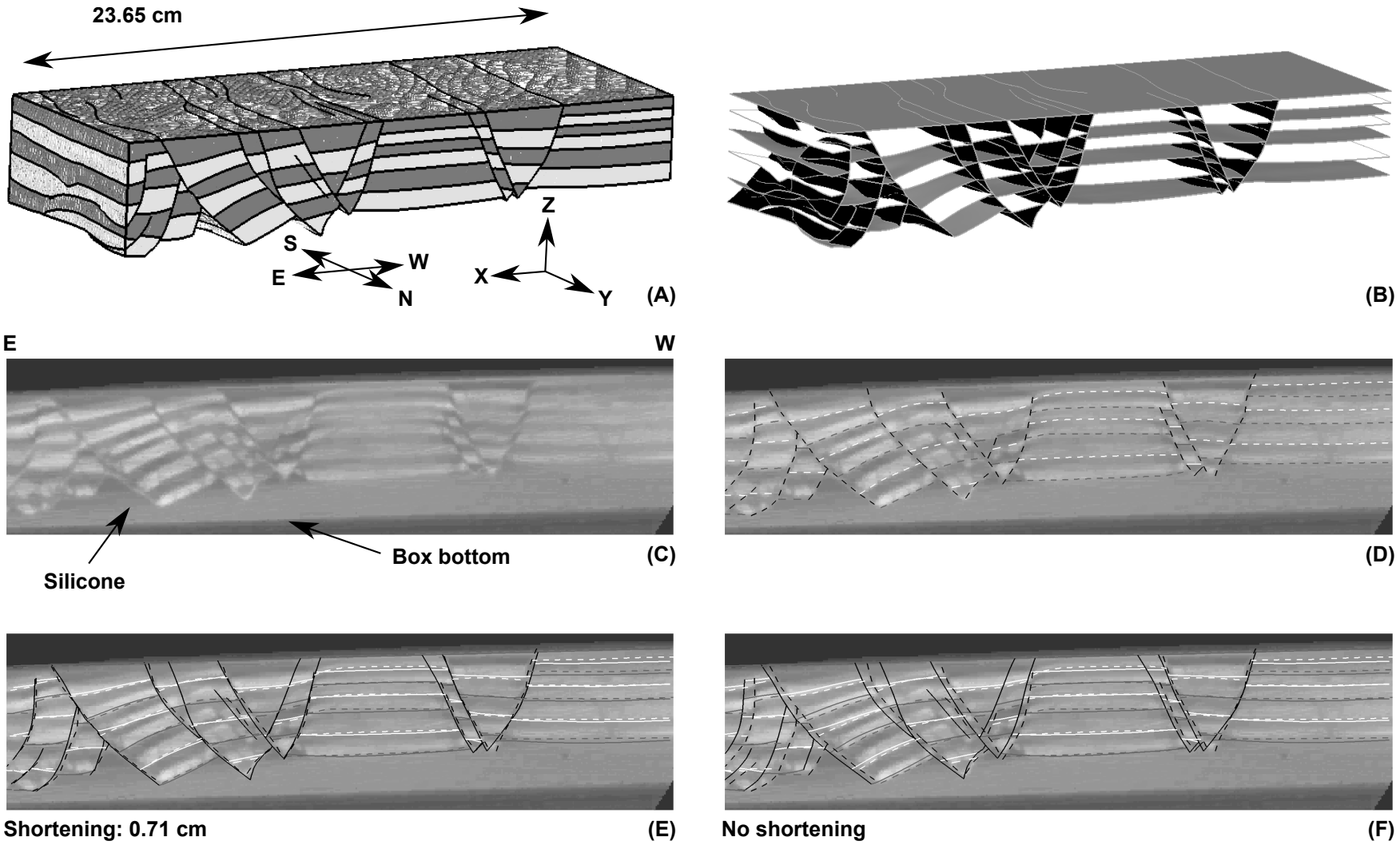

Figure 10: (A) Restored volumetric model obtained with a shortening of 0.71 cm. (B) Restored surface model obtained with a shortening of 0.71 cm. (C) Uninterpreted CT image of the northern edge at H7 deposition time. (D) Interpreted CT image of the northern edge at H7 deposition time (dashed curves). The interpretation represents the reference solution. (E) Same as (D) with the restoration result with a shortening boundary condition of 0.71 cm (continuous curves). (F) Same as (D) with the restoration result without shortening boundary condition for this restoration step (continuous curves). The unrestored model is the restored model at the first restoration step with a shortening boundary condition of 1.44 cm (Figure 9E). CT data courtesy of IFPEN and C&C Reservoirs, 2016, DAKS^{TM} - Digital Analogs Knowledge System.

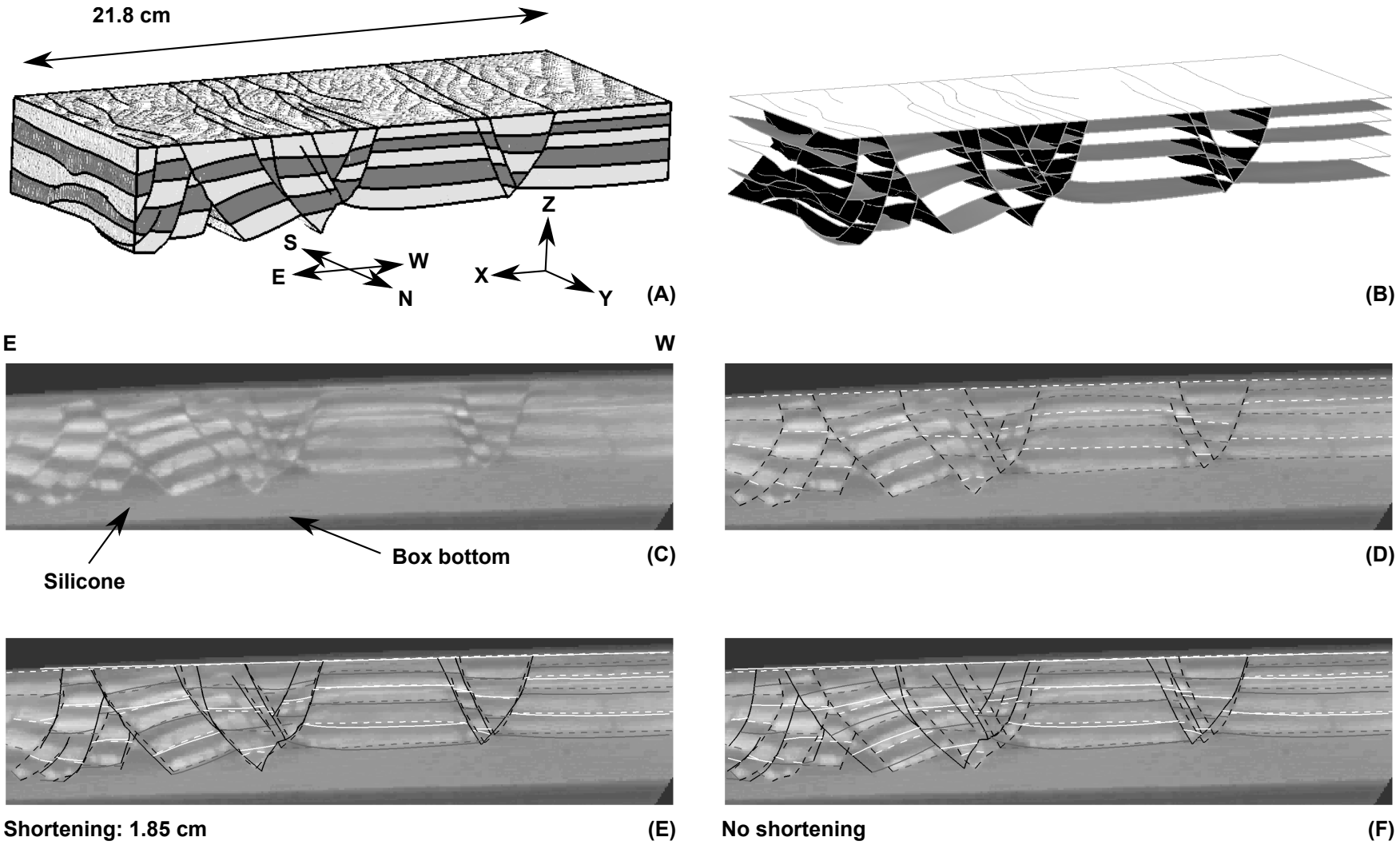

Figure 11: (A) Restored volumetric model obtained with a shortening of 1.85 cm. (B) Restored surface model obtained with a shortening of 1.85 cm. (C) Uninterpreted CT image of the northern edge at H6 deposition time. (D) Interpreted CT image of the northern edge at H6 deposition time (dashed curves). The interpretation represents the reference solution. (E) Same as (D) with the restoration result with a shortening boundary condition of 1.85 cm (continuous curves). (F) Same as (D) with the restoration result without shortening boundary condition for this restoration step (continuous curves). The unrestored model is the restored model at the second restoration step with a shortening boundary condition of 0.71 cm (Figure 10E). CT data courtesy of IFPEN and C&C Reservoirs, 2016, DAKS^{TM} - Digital Analogs Knowledge System.

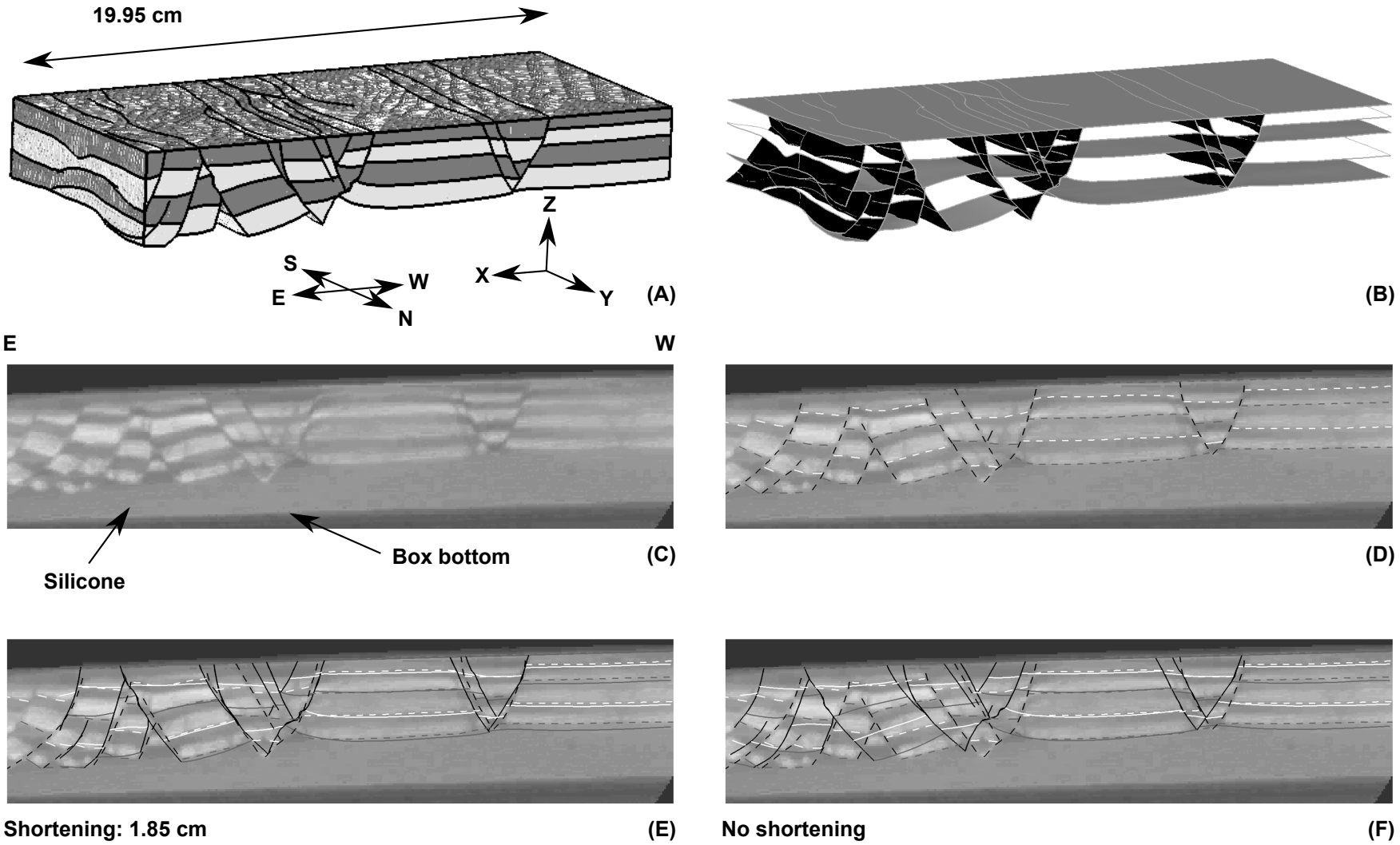

Figure 12: (A) Restored volumetric model obtained with a shortening of 1.85 cm. (B) Restored surface model obtained with a shortening of 1.85 cm. (C) Uninterpreted CT image of the northern edge at H5 deposition time. (D) Interpreted CT image of the northern edge at H5 deposition time (dashed curves). The interpretation represents the reference solution. (E) Same as (D) with the restoration result with a shortening boundary condition of 1.85 cm (continuous curves). (F) Same as (D) with the restoration result without shortening boundary condition for this restoration step (continuous curves). The unrestored model is the restored model at the third restoration step with a shortening boundary condition of 1.85 cm (Figure 11E). CT data courtesy of IFPEN and C&C Reservoirs, 2016, DAKS^{TM} - Digital Analogs Knowledge System.

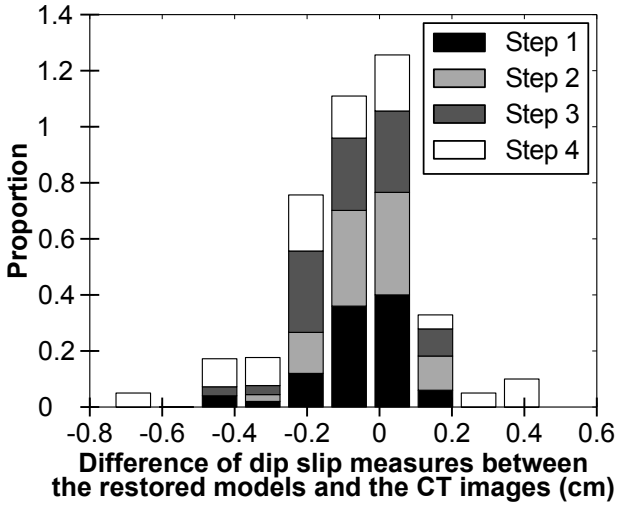

Figure 13: Difference of dip slip measures between the restored model and the reference for the first four restoration steps (with shortenings). For all the restoration steps except the fourth one, the majority of the dip slip deltas is within the uncertainty range (-0.2 cm and 0.2 cm).

3.2 Validation: quantitative comparison with a reference solution

The visual comparison of the restored models with the references provides valuable insight on the quality of our restorations. However, quantitative analysis is necessary to rigorously and objectively assess the restoration quality (Lingrey and Vidal-Royo, 2015, 2016) and uncertainties. To quantify the difference between the restored models and the reference paleo-geometries, we measured the magnitude of residual dip slip along faults after a restoration step. Dip slip provides a quantitative measure of the recovered strain along each fault. For each fault that crosses the northern edge, we measured the amount of offset for each horizon on the CT pictures. In addition, we computed the dip slip values on each fault in the numerical models at the considered time steps. The difference of dip slip values between the restored model and the reference, that we call *delta*, is calculated as

$$delta = DS^{res} - DS^{ref}, \tag{1}$$

with DS^{res} and DS^{ref} respectively the dip slip in the restored state and the dip slip on the reference CT image. The corresponding distributions for the first four restoration steps (with shortening boundary conditions) are shown in Figure 13. To avoid bias in this analysis, these distributions do not include the dip slip measures at the uppermost horizon, as these dip slip values are defined by input boundary conditions (Figure 5E). Table 2 presents the mean and median values for each dip slip delta distribution shown in Figure 13, as well as the percentage of dip slip deltas within the picking uncertainty range estimated to be between -0.2 cm (-0.08 in) and +0.2 cm (+0.08 in). This uncertainty value originates from the picking uncertainty (0.1 cm) applied on the footwall and the hanging wall. It also considers similar uncertainties in our interpretations of paleo-geometries and dip slip magnitudes on the CT images. The distributions show maxima near zero delta. In addition, the majority of the residual dip slip measurements are within the uncertainty range considered (Table 2). Therefore, we suggest these restorations, which each included the applied shortening boundary condition to the down-dip model wall, are valid. Nevertheless, some slip measurements from restoration models differ significantly from the reference solution. These are clearly not a common result, except in the fourth restoration step (white intervals in Figure 13, Table 2, see discussions).

4 Estimation of shortening

As shown previously, the amount of extension that is restored without the applied boundary condition to the down-dip model wall consistently underestimates the actual amount of extension that occurred in the forward model. For natural structures, the total amount of extension (or shortening) that occurred to yield the present-day geometry is generally unknown. In these cases, an estimation of the amount of displacement can be attempted using 2D kinematic restoration approaches (e.g., Chamberlin, 1910; Dahlstrom, 1969) or 2D area-depth analysis (Epard and Groshong, 1993; Groshong et al., 2003; Groshong, 2006; Groshong et al., 2012). Specific markers, such as channel offsets, can be used if present as proposed by Durand-Riard et al. (2013b).

Restoration step	1	2	3	4
Dip slip deltas (%) between -0.2 cm (-0.8 in) and 0.2 cm (0.8 in)	82	88	87	50
Mean in cm (in)	-0.059 (-0.023)	-0.043 (-0.017)	-0.075 (-0.030)	-0.094 (-0.037)
Median in cm (in)	-0.027 (-0.011)	-0.038 (-0.015)	-0.07 (-0.028)	-0.102 (-0.0402)

Table 2: For each restoration step, the mean and the median of the dip slip delta distribution (Figure 13) are indicated, in addition to the percentage of dip slip deltas within the picking uncertainty range.

	Horizon	H8	H7	H6	H5
Incremental shortenings in cm (in, %) estimated by different methods	CT image	1.44 (0.567, 100%)	0.71 (0.28, 100%)	1.85 (0.728, 100%)	1.85 (0.728, 100%)
	Area-depth	1.452 (0.5717, 101%)	0.806 (0.317, 114%)	1.807 (0.7114, 98%)	1.614 (0.6354, 87%)
	Fault heave sum	0.676 (0.266, 47%)	0.436 (0.172, 61%)	1.056 (0.4157, 57%)	0.602 (0.237, 33%)
	Bed length conservation	0.597 (0.235, 41%)	0.257 (0.101, 36%)	0.922 (0.363, 50%)	0.495 (0.195, 27%)
	No imposed shortening condition	0.718 (0.283, 50%)	0.345 (0.136, 49%)	0.834 (0.328, 45%)	0.459 (0.181, 25%)

Table 3: For each restoration step, several geometric methods are used, in addition to the measure on CT images, to assess the shortening magnitude (see text for details). Each percentage is relative to the corresponding reference shortening measured on the CT image.

4.1 Methods based on rigid motion and bed length conservation

Table 3 presents the incremental shortening evaluated by different methods, in particular fault heave and bed length conservation. The former corresponds to the required horizontal displacement to tie the uppermost horizon parts as a pure rigid motion of the fault blocks. The latter, in addition to joining the uppermost horizon parts, assumes that this horizon conserves its bed length and is restored to horizontal. In this case, the horizontal displacement is equal to the horizontal extension of the analog model in the X direction (i.e., down-dip direction) before restoration minus the sum of the lengths of the uppermost horizon parts. For each of these two methods, we used the unrestored model (with applied shortening boundary condition) geometry at each restoration step. Both methods provide displacement estimates that are significantly less than the expected values (Table 3). In other words, rigid motion along faults is not an accurate measure of total tectonic displacement for our model and bed lengths did not remain constant through deformation. This latter conclusion is a known expectation for extensional structures (e.g., Xiao and Suppe, 1992). There is internal deformation accommodated by structures below image resolution or by deformation of a more continuous nature.

4.2 Area-depth method

We applied the area-depth method (Epard and Groshong, 1993; Groshong et al., 2003; Groshong, 2006; Groshong et al., 2012) to estimate the total forward extension without the need of a reference paleo-geometry. The area-depth method may be used to calculate the magnitude of shortening or extension of a system above a basal detachment. A benefit of this method is that it accounts for the displacement due to faults omitted from the interpretation or tectonic strain that is below our imaging resolution, which has been found to accommodate up to 60% of total extension within a given system (e.g., Kautz and Sclater, 1988; Marrett and Allmendinger, 1992; Baxter, 1998; Groshong et al., 2003). The area-depth method is independent of the mechanical processes and is based on assumptions of area conservation and plane-strain, given that a thin detachment level exists. The area-depth method defines for each horizon a regional depth of detachment and a lost area inside the graben (below the regional datum and above the horizon), as shown in Figure 14. This lost area is equal to the product of the displacement that produced the graben and the depth to the detachment level. It follows that the total extension is given by the lost area divided by the depth to the detachment. We did not plot an area-depth

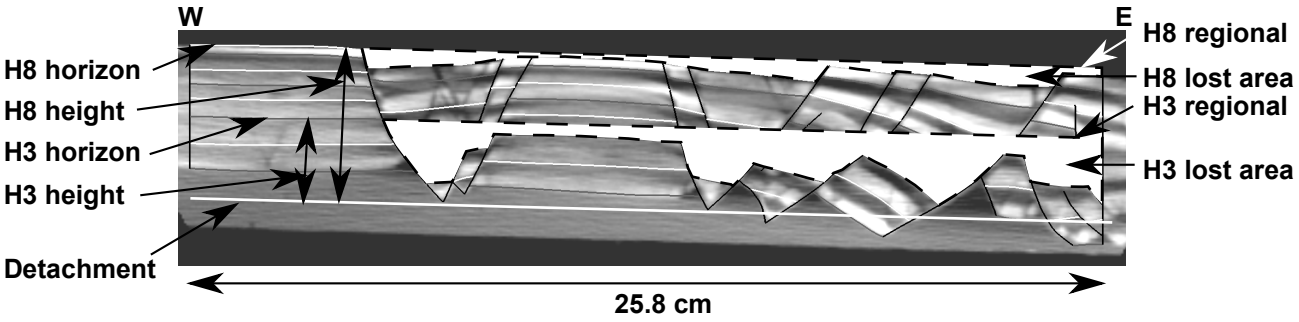

Figure 14: Area-depth method applied on the north CT image at the final stage of the structural sandbox experiment. Examples of the calculus for two horizons: H8 and H3. For each horizon a lost area (white area with dashed border line) is computed. The lost area for a horizon is the area above this horizon and below the regional level of this horizon. The height to the detachment is computed for each horizon. Total shortening (from the beginning of the deformation) undergone by a horizon is its lost area divided by its height to the detachment. CT data courtesy of IFPEN and C&C Reservoirs, 2016, DAKS^{TM} - Digital Analogs Knowledge System.

graph of the entire growth sequence, which would integrate each lost area and each distance from the regional to a reference level, since by definition the layers did not undergo the same magnitude of extension (Groshong et al., 2003). Indeed, such a plot enables to evaluate the common displacement and the depth to detachment only for pregrowth strata or for no-growth sequences of growth strata (Groshong, 2015). Thus, we assume that the depth to the detachment is known. In our analog model, the definition of the detachment level is not straightforward, as the silicone layer is thick and may act as a distributed detachment zone. Assuming that no slip occurs along silicone boundaries (Weijermars et al., 1993), we approximated the detachment level to be at the middle of the silicone layer (Figure 14). The regional level of each horizon is defined by a straight line dipping 1.5° (parallel to the detachment) and starting from the intersection between the horizon and the most western fault (Figure 14). Our calculations only use the north CT image of the analog final deformation stage. The estimates of the shortening magnitude increments for the first four horizons using the area-depth method and the CT images are given in Table 3. The amounts of displacement predicted by the area-depth method are within 15% of the shortening magnitudes provided by the CT images. We consider this a valid estimate given the structural uncertainties.

4.3 3D dilatation analysis

We propose a complementary approach to evaluate the model forward extension from calculations of dilatation, where

$$dilatation = 100 \times \frac{V^r - V^u}{V^u}, \tag{2}$$

with V^r and V^u respectively the restored volume and the unrestored volume. As previously discussed, horizontal dilatation is expected during the experiment. Due to the small duration and the scale of the experiment, the strata used in our model are not expected to undergo significant vertical compaction (Schultz-Ela, 1992). Thus, we expect the volume to increase during forward deformation experiment. A consequence is that the volume should decrease during restoration, resulting in negative dilatation calculations from Equation (2). We ran a large number of geomechanical restorations varying the magnitude of shortening imposed as a boundary condition. Figure 15 represents the proportion of tetrahedra with a positive dilatation from the unrestored state to the restored state according to magnitudes of the imposed shortening conditions. In this way, we attempt to estimate the magnitude of shortening required to minimize the number of tetrahedra with positive dilatation. Similarly, Durand-Riard (2010), with a contractional model, used a lateral (elongation) displacement to reduce the number of tetrahedra with a negative dilatation. The shortenings in Table 3 are displayed in the different graphs of Figure 15. As expected, the number of tetrahedra with a positive dilatation decreases when the magnitude of the applied shortening increases. However, in each scenario (Figure 15), a plateau of diminishing returns develops with additional applied shortening. The beginning of each plateau, as well as the area-depth estimates, provides a much improved estimate of the shortening magnitude than the other methods investigated above (Table 3). While this conclusion is still empirical, we suggest that dilatation may be an effective tool to estimate the magnitude of the lateral displacement boundary condition and to evaluate the validity of the restored state.

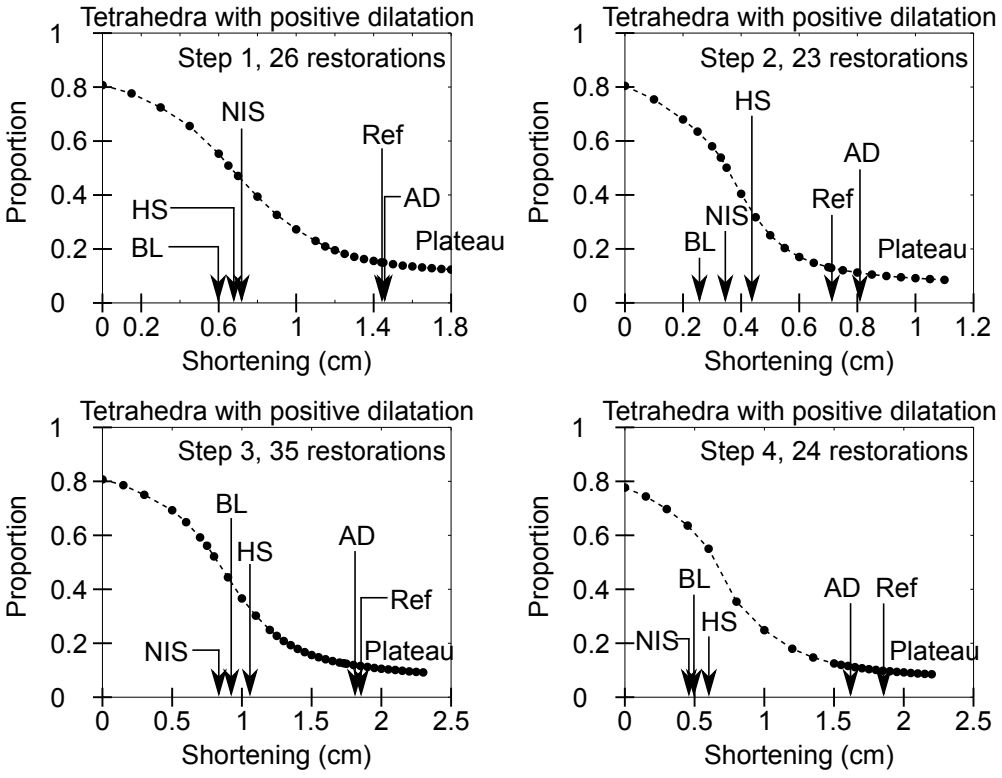

Figure 15: Proportion of tetrahedra with a positive dilatation after each restoration step (steps 1 to 4) according to different shortenings (in centimeters). Black dots are data points (restoration simulations). For each restoration, the unrestored state is the restored state at the previous restoration step with the imposed shortening from CT image (and without the uppermost restored layer). Shortenings in Table 3 are displayed on each graph. Ref: shortening from the CT image. AD: shortening from the area-depth method. HS: sum of the fault heaves of uppermost horizon fault cutoff lines on the northern wall. BL: shortening from the bed length conservation method. NIS: no imposed shortening on the northern wall (restoration without shortening condition).

Restoration step	1	2	3	4
Forward dilatation of sand and pyrex strata (%)	3.38	0.73	3.07	3.64

Table 4: See Equation (3) and text for calculation details. The forward dilatation of sand and pyrex strata for each restoration step is positive, testifying an increase of area forward in time.

5 Discussions

5.1 Reasons for a shortening boundary condition

There are several potential explanations for the requirement of an imposed shortening boundary condition. A first reason is the granular nature of the growth strata. According to Groshong et al. (2003); Yamada and McClay (2003); Le Guerroué and Cobbold (2006), and Moretti and Callot (2012), dilatation is likely to occur in structural sandbox models when granular materials undergo shear. This effect enables faults to develop in unconsolidated materials (e.g., Colletta et al., 1991; Cobbold and Castro, 1999; Le Guerroué and Cobbold, 2006; Groshong et al., 2012). As deformation progresses, additional shear occurs and more voids develop in the system (Groshong et al., 2003; Le Guerroué and Cobbold, 2006). This disorder is at the origin of an increase of the global volume, and thus must be countered by applied shortening in the restoration. Table 4 provides the forward dilatation ϵ_v (volumetric strain) of the sand and pyrex strata measured on the CT images for each restoration step using

$$\epsilon_v = 100 \times \frac{\left(A_i^d - A_i^u\right)}{A_i^u}, \tag{3}$$

with A_i^u and A_i^d respectively the area of the sand and pyrex strata on the CT image at deposition time of the layer i and just before the deposition of the layer just above the layer i. At each step, the forward dilatation is positive, which means the analog model area on the northern edge increased through time. Nevertheless, we have just such an evidence of dilatation on the northern edge thanks to the CT images; this dilatation may or may not be compensated elsewhere within the volume. However, due to the style of deformation of the sandbox model, it is very probable that the forward dilatation observed on the CT images is representative of the entire volume. Rock dilatation may exist in real extensional fields in which sediments contain fluids (e.g., Boerner and Sclater, 1992). Another important reason which explains the need for the shortening boundary condition is that a part of the fault displacement may not be taken into account. Indeed, all the observed faults are not represented, and there may be faults below tomography resolution. Even if their offsets are small, accumulated fault heaves may represent significant forward extension. This is analogous to nature with faults below seismic resolution, which are not imaged and, thus, unable to be represented at the macro-scale (e.g., Groshong et al., 2003).

5.2 Residual amounts of fault dip slip values

Although the distributions in Figure 13 are encouraging, the number of inconsistent fault dip slip deltas increases with each successive restoration step. A possible explanation for this is that each residual dip slip on these faults is not corrected between restoration steps to fit the dip slip observed on CT images, leading to the accumulation of errors. Another possible explanation is that some faults are kept within the volumetric model whereas they were not present in the analog model at the time corresponding to the restoration step. As faults behave as sliding surfaces in our volumetric mesh, small artificial slip may be present on these surfaces, leading to local inconsistent shear strain. We kept these faults to avoid rebuilding a new structural model, which can be quite time-intensive for such complex fault networks (Zehner et al., 2015). Another observation of these distributions suggests that the restorations seemed to have recovered too much dip slip (numerous negative deltas). Since the forward deformation path involves friction on faults, this result may be due to the frictionless contacts in our mechanics-based restoration method (Wriggers and Laursen, 2006).

5.3 Mismatches with the area-depth method

As mentioned previously, the area-depth method provides a reasonable estimate of the incremental extension that occurred during the forward model (Table 3). However, the estimates are not perfect, in particular for the restoration step 4 (Figures 12 and 15). Several factors may explain these errors. First, material dilatation observed on the CT images and attested by several authors (Yamada and McClay, 2003; Le Guerroué and Cobbold, 2006) is inconsistent with the area conservation hypothesis underlying the area-depth method. As

the upper horizons have accumulated less dilatation than the bottom horizons, the constant area hypothesis deteriorates with each successive restoration step. Second, the silicone layer could migrate laterally and blend with the sand and pyrex, leading to area changes. In the analog model, from the CT image of the restoration step 4 to the CT image representing the first unrestored state (northern edge), we calculated a forward dilatation of the silicone to ∼6.8%. Third, as a part of the analog model on the eastern side was not available for analysis in our CT tomography images, we could not integrate this data in our area-depth computations. Fourth, the definition of the detachment level, even based on several reasonable assumptions, is uncertain. Fifth, as the units of sand and pyrex can penetrate into the silicone, the resulting subsidence modifies the definition of the regional levels. This effect is equivalent to the "floating regional" mentioned by Groshong (2015) for a buckle-style fold above a thick salt unit.

5.4 Boundary conditions

This study suggests that for extensional systems, the combination of classical boundary conditions and a new lateral displacement boundary condition along the dominant transport direction (Figure 5) may yield consistent restored geometries. In this paper, we also propose the use of novel contact conditions to ensure consistent restoration of complex branching and crossing fault geometries. These new constraints enable effective sequential restoration of four steps of the analog model. Without them, only two steps could have been performed, and quality of these restorations would have been reduced. We believe that the boundary conditions presented in Figure 5 can be applied in compressive contexts with an elongation displacement condition instead of the shortening condition. Indeed, Durand-Riard (2010) shows that an elongation condition is necessary to properly restore a fault-bend fold model. An estimation of the elongation may be done using the area-depth method (Groshong et al., 2012). In case of strike-slip faults, displacement conditions parallel to the strike direction should also be considered, as shown by Durand-Riard et al. (2013b).

In the literature and in this paper, all the boundary conditions correspond to displacement conditions except for the mechanical contact conditions which are a mix between displacement and traction conditions (Muron, 2005; Wriggers and Laursen, 2006; Maerten and Maerten, 2006). Such displacement conditions may lead to unphysical strain fields (Lovely et al., 2012). In reality, rock deformation is a consequence of force constraints. Maerten and Maerten (2006) suggest the possibility of employing mechanical boundary conditions that incorporate the far field stress as an additional boundary condition. The main difficulty of this technique would be to know the intensity of the forces to apply (Muron, 2005). A first start could be to use the determined displacement condition for a model (e.g., Figure 15) and convert it to a force: dilatation multiplied by Young's modulus in linear elasticity. In addition, the overburden force is not incorporated in our geomechanical restoration method. As our experiment was gravity-driven, it would be interesting to add an overburden body force to the finite element procedure to analyze its impact on the restored geometries.

Conclusions

The restoration of an analog model, in which the structural uncertainties are limited and paleo-geometry is well known, enabled us to define effective boundary conditions that yield optimal restored models using mechanics-based restoration. For extensional structures, a shortening boundary condition was applied to obtain a good fit with reference paleo-geometries. Such a condition may be estimated by the area-depth method. Our experiments suggest that an analysis of the volumetric dilatation can complement the estimate of the shortening boundary condition magnitude. Moreover, to handle complex fault networks, we propose the application of contact conditions on internal fault borders and between fault connected components. Ultimately, the methods developed in this paper, in particular the lateral displacement boundary condition, should lead to improved results if applied to geomechanical restorations of natural structures.

Ackowledgements

This work was performed as part of the RING project at Université de Lorraine. We would like to thank the industrial and academic sponsors of the RING-GOCAD Consortium managed by ASGA for their support, and Chevron for funding the Ph.D. of Benjamin Chauvin. We also acknowledge Paradigm for the SKUA-GOCAD software and API, and Inria for the Geogram library used in RINGMesh. We thank IFPEN and C&C Reservoirs, DAKS^{TM} - Digital Analog Knowledge System, for the analog model data set. We also acknowledge Justin Herbert, Donald Medwedeff and Richard Groshong for discussions, feedback and involvement in this

work. Frantz Maerten, Robert Worthington and Frank Zwaan provided helpful comments that improved the quality of this manuscript.

References

K. Baxter. The role of small-scale extensional faulting in the evolution of basin geometries. An example from the late Palaeozoic Petrel Sub-basin, northwest Australia. *Tectonophysics*, 287(1): 21–41, 1998. doi: 10.1016/S0040-1951(98)80059-0.

T. Belytschko, W. K. Liu, B. Moran, and K. Elkhodary. *Nonlinear finite elements for continua and structures*. John Wiley & Sons, Chichester, United Kingdom, 2nd edition, 2013.

S. T. Boerner and J. G. Sclater. Deformation under extension of assemblies of steel balls in contact: application to sandbox models. *Journal of Geophysical Research: Solid Earth*, 97(B4): 4969–4990, 1992. doi: 10.1029/91JB02274.

C. E. Bond. Uncertainty in structural interpretation: Lessons to be learnt. *Journal of Structural Geology*, 74: 185–200, 2015. doi: 10.1016/j.jsg.2015.03.003.

C. E. Bond, A. D. Gibbs, Z. K. Shipton, and S. Jones. What do you think this is? "Conceptual uncertainty" in geoscience interpretation. *GSA today*, 17(11): 4–10, 2007. doi: 10.1130/GSAT01711A.1.

A. Botella. *Génération de maillages non structurés volumiques de modèles géologiques pour la simulation de phénomènes physiques*. PhD thesis, Université de Lorraine, 2016a.

A. Botella. VorteXLib, 2016b. URL `http://www.ring-team.org/software/ring-libraries/45-vortexlib`.

A. Botella, J. Pellerin, A. Mazuyer, B. Chauvin, F. Bonneau, P. Anquez, and M. Raguenel. RINGMesh, 2016. URL `http://www.ring-team.org/software/ringmesh`.

J.-P. Callot, V. Trocmé, J. Letouzey, E. Albouy, S. Jahani, and S. Sherkati. Pre-existing salt structures and the folding of the Zagros Mountains. *Geological Society, London, Special Publications*, 363(1): 545–561, 2012. doi: 10.1144/SP363.27.

G. Caumon, F. Lepage, C. H. Sword, and J.-L. Mallet. Building and Editing a Sealed Geological Model. *Mathematical Geology*, 36(4): 405–424, 2004. doi: 10.1023/B:MATG.0000029297.18098.8a.

R. T. Chamberlin. The Appalachian folds of central Pennsylvania. *The Journal of Geology*, 18(3): 228–251, 1910. doi: 10.1086/621722.

B. Chauvin and A. Mazuyer. RINGMecha, 2016. URL `http://www.ring-team.org/software/ring-libraries/44-ringmecha`.

N. Cherpeau and G. Caumon. Stochastic structural modelling in sparse data situations. *Petroleum Geoscience*, 21(4): 233–247, 2015. doi: 10.1144/petgeo2013-030.

P. R. Cobbold and L. Castro. Fluid pressure and effective stress in sandbox models. *Tectonophysics*, 301(1): 1–19, 1999. doi: 10.1016/S0040-1951(98)00215-7.

B. Colletta, J. Letouzey, R. Pinedo, J.-F. Ballard, and P. Balé. Computerized X-ray tomography analysis of sandbox models: Examples of thin-skinned thrust systems. *Geology*, 19(11): 1063–1067, 1991. doi: 10.1130/0091-7613(1991)019<1063:CXRTAO>2.3.CO;2.

C. D. A. Dahlstrom. Balanced cross sections. *Canadian Journal of Earth Sciences*, 6(4): 743—-757, 1969. doi: 10.1139/e69-069.

R. Darnault, J.-P. Callot, J.-F. Ballard, G. Fraisse, J.-M. Mengus, and J.-C. Ringenbach. Control of syntectonic erosion and sedimentation on kinematic evolution of a multidecollement fold and thrust zone: Analogue modeling of folding in the southern subandean of Bolivia. *Journal of Structural Geology*, 89: 30–43, 2016. doi: 10.1016/j.jsg.2016.05.009.

T. P. Dooley, M. Jackson, and M. R. Hudec. Initiation and growth of salt-based thrust belts on passive margins: results from physical models. *Basin Research*, 19(1): 165–177, 2007. doi: 10.1111/j.1365-2117.2007.00317.x.

J. A. Dunbar and R. W. Cook. Palinspastic reconstruction of structure maps: an automated finite element approach with heterogeneous strain. *Journal of Structural Geology*, 26: 1021–1036, 2003. doi: 10.1016/S0191-8141(02)00154-2.

P. Durand-Riard. *Gestion de la complexité géologique en restauration géomécanique 3D*. PhD thesis, Institut National Polytechnique de Lorraine, 2010.

P. Durand-Riard, G. Caumon, and P. Muron. Balanced restoration of geological volumes with relaxed meshing constraints. *Computers & Geosciences*, 36(4): 441–452, 2010. ISSN 00983004. doi: 10.1016/j.cageo.2009.07.007.

P. Durand-Riard, C. A. Guzofski, G. Caumon, and M.-O. Titeux. Handling natural complexity in three-dimensional geomechanical restoration, with application to the recent evolution of the outer fold and thrust belt, deep-water Niger Delta. *AAPG bulletin*, 97(1): 87–102, 2013a. doi: 10.1306/06121211136.

P. Durand-Riard, J. H. Shaw, A. Plesch, and G. Lufadeju. Enabling 3D geomechanical restoration of strike- and oblique-slip faults using geological constraints, with applications to the deep-water Niger Delta. *Journal of Structural Geology*, 48: 33–44, 2013b. doi: 10.1016/j.jsg.2012.12.009.

P. G. Ellis and K. R. McClay. Listric extensional fault systems - results of analogue model experiments. *Basin Research*, 1(1): 55–70, 1988. doi: 10.1111/j.1365-2117.1988.tb00005.x.

J.-L. Epard and R. H. Groshong. Excess area and depth to detachment. *AAPG bulletin*, 77(8): 1291–1302, 1993.

R. C. Fletcher and D. D. Pollard. Can we understand structural and tectonic processes and their products without appeal to a complete mechanics? *Journal of Structural Geology*, 21: 1071–1088, 1999. ISSN 01918141. doi: 10.1016/S0191-8141(99)00056-5.

R. Frodeman. Geological reasoning: Geology as an interpretive and historical science. *Geological Society of America Bulletin*, 107(8): 960–968, 1995. doi: 10.1130/0016-7606(1995)107<0960:GRGAAI>2.3.CO;2.

J.-P. Gratier, B. Guillier, A. Delorme, and F. Odonne. Restoration and balance of a folded and faulted surface by best-fitting of finite elements: principle and applications. *Journal of Structural Geology*, 13(1): 111–115, 1991. doi: 10.1016/0191-8141(91)90107-T.

P. Griffiths, S. Jones, N. Salter, F. Schaefer, R. Osfield, and H. Reiser. A new technique for 3-D flexural-slip restoration. *Journal of Structural Geology*, 24(4): 773–782, 2002. doi: 10.1016/S0191-8141(01)00124-9.

R. H. Groshong. *3-D structural geology*. Springer, 2006. doi: 10.1007/978-3-540-31055-6.

R. H. Groshong. Quality control and risk assessment of seismic profiles using area-depth-strain analysis. *Interpretation*, 3(4): SAA1—-SAA15, 2015. doi: 10.1190/INT-2015-0010.1.

R. H. Groshong, J. C. Pashin, B. Chai, and R. D. Schneeflock. Predicting reservoir-scale faults with area balance: Application to growth stratigraphy. *Journal of Structural Geology*, 25(10): 1645–1658, 2003. doi: 10.1016/S0191-8141(03)00002-6.

R. H. Groshong, M. O. Withjack, R. W. Schlische, and T. N. Hidayah. Bed length does not remain constant during deformation: recognition and why it matters. *Journal of Structural Geology*, 41: 86–97, 2012. doi: 10.1016/j.jsg.2012.02.009.

C. A. Guzofski, J. P. Mueller, J. H. Shaw, P. Muron, D. A. Medwedeff, F. Bilotti, and C. Rivero. Insights into the mechanisms of fault-related folding provided by volumetric structural restorations using spatially varying mechanical constraints. *AAPG Bulletin*, 93(4): 479–502, 2009. ISSN 01491423. doi: 10.1306/11250807130.

T. Hidayah. Experimental modeling of focused shortening: Understanding the structural development of reverse fault zones, 2010.

R. Holtzman, D. B. Silin, and T. W. Patzek. Mechanical properties of granular materials: A variational approach to grain-scale simulations. *International journal for numerical and analytical methods in geomechanics*, 33 (3): 391–404, 2009. doi: 10.1002/nag.725.

M. K. Hubbert. Theory of scale models as applied to the study of geologic structures. *Geological Society of America Bulletin*, 48(10): 1459–1520, 1937. doi: 10.1130/GSAB-48-1459.

S. A. Kautz and J. G. Sclater. Internal deformation in clay models of extension by block faulting. *Tectonics*, 7 (4): 823–832, 1988. doi: 10.1029/TC007i004p00823.

E. Le Guerroué and P. R. Cobbold. Influence of erosion and sedimentation on strike-slip fault systems: insights from analogue models. *Journal of Structural Geology*, 28(3): 421–430, 2006. doi: 10.1016/j.jsg.2005.11.007.

M. Léger, M. Thibaut, J.-P. Gratier, and J.-M. Morvan. A least-squares method for multisurface unfolding. *Journal of structural geology*, 19(5): 735–743, 1997. doi: 10.1016/S0191-8141(97)85678-7.

B. Lévy. Geogram, 2015. URL `http://alice.loria.fr/index.php/software/4-library/75-geogram.html`.

S. Lingrey and O. Vidal-Royo. Evaluating the quality of bed length and area balance in 2D structural restorations. *Interpretation*, 3(4): SAA133—-SAA160, 2015. doi: 10.1190/INT-2015-0126.1.

S. Lingrey and O. Vidal-Royo. Evaluating a 2-D Structural Restoration: Validating Section Balance. In *AAPG Search and Discovery article 41941*, 2016.

P. Lovely, E. Flodin, C. A. Guzofski, F. Maerten, and D. D. Pollard. Pitfalls among the promises of mechanics-based restoration: Addressing implications of unphysical boundary conditions. *Journal of Structural Geology*, 41: 47–63, 2012. ISSN 01918141. doi: 10.1016/j.jsg.2012.02.020.

F. Maerten and L. Maerten. Unfolding and Restoring Complex Geological Structures Using Linear Elasticity Theory. In *AGU Fall Meeting Abstracts*, vol. 1, p. 940, 2001.

F. Maerten and L. Maerten. On a method for reducing interpretation uncertainty of poorly imaged seismic horizons and faults using geomechanically based restoration technique. *Interpretation*, 3(4): SAA105—-SAA116, 2015. doi: 10.1190/INT-2015-0009.1.

L. Maerten and F. Maerten. Chronologic modeling of faulted and fractured reservoirs using geomechanically based restoration: Technique and industry applications. *AAPG Bulletin*, 90(8): 1201—-1226, 2006. doi: 10.1306/02240605116.

R. Marrett and R. W. Allmendinger. Amount of extension on "small" faults: An example from the Viking graben. *Geology*, 20(1): 47–50, 1992. doi: 10.1130/0091-7613(1992)020<0047:AOEOSF>2.3.CO;2.

K. R. McClay. Extensional fault systems in sedimentary basins: a review of analogue model studies. *Marine and Petroleum Geology*, 7(3): 206–233, 1990. doi: 10.1016/0264-8172(90)90001-W.

P. Mejía-Herrera, J.-J. Royer, G. Caumon, and A. Cheilletz. Curvature attribute from surface-restoration as predictor variable in Kupferschiefer copper potentials. *Natural Resources Research*, 24(3): 275–290, 2014. doi: 10.1007/s11053-014-9247-7.

I. Moretti. Working in complex areas: New restoration workflow based on quality control, 2D and 3D restorations. *Marine and Petroleum Geology*, 25(3): 205–218, 2008. ISSN 02648172. doi: 10.1016/j.marpetgeo.2007.07.001.

I. Moretti and J.-P. Callot. Area, length and thickness conservation: Dogma or reality? *Journal of Structural Geology*, 41: 64–75, 2012. doi: 10.1016/j.jsg.2012.02.014.

I. Moretti, F. Lepage, and M. Guiton. KINE3D: a new 3D restoration method based on a mixed approach linking geometry and geomechanics. *Oil & Gas Science and Technology*, 61(2): 277–289, 2006. doi: 10.2516/ogst:2006021.

T. Munson. Mesh shape-quality optimization using the inverse mean-ratio metric. *Mathematical Programming*, 110(3): 561–590, 2007. doi: 10.1007/s10107-006-0014-3.

P. Muron. *Méthodes numériques 3-D de restauration des structures géologiques faillées*. PhD thesis, Institut National Polytechnique de Lorraine, 2005.

M. Panien, G. Schreurs, and A. Pfiffner. Mechanical behaviour of granular materials used in analogue modelling: insights from grain characterisation, ring-shear tests and analogue experiments. *Journal of Structural Geology*, 28(9): 1710–1724, 2006. doi: 10.1016/j.jsg.2006.05.004.

Paradigm. SKUA-GOCAD, 2015. URL `http://www.pdgm.com/products/skua-gocad/`.

V. N. Parthasarathy, C. M. Graichen, and A. F. Hathaway. A comparison of tetrahedron quality measures. *Finite Elements in Analysis and Design*, 15(3): 255–261, 1994. doi: 10.1016/0168-874X(94)90033-7.

J. Pellerin, B. Lévy, G. Caumon, and A. Botella. Automatic surface remeshing of 3D structural models at specified resolution: A method based on Voronoi diagrams. *Computers & Geosciences*, 62: 103–116, 2014. ISSN 0098-3004. doi: 10.1016/j.cageo.2013.09.008.

J. Pellerin, G. Caumon, C. Julio, P. Mejía-Herrera, and A. Botella. Elements for measuring the complexity of 3D structural models: Connectivity and geometry. *Computers & Geosciences*, 76(0): 130–140, 2015. ISSN 0098-3004. doi: 10.1016/j.cageo.2015.01.002.

J. Pellerin, A. Botella, F. Bonneau, A. Mazuyer, B. Chauvin, B. Lévy, and G. Caumon. RINGMesh: A programming library for developing mesh-based geomodeling applications. *Computers & Geosciences*, 104: 93–100, 2017. doi: 10.1016/j.cageo.2017.03.005.

A. Plesch, J. H. Shaw, and D. Kronman. Mechanics of low-relief detachment folding in the Bajiaochang field, Sichuan Basin, China. *AAPG bulletin*, 91(11): 1559–1575, 2007. doi: 10.1306/06200706072.

H. Ramberg. *Gravity, deformation, and the earth's crust: In theory, experiments, and geological application*. Academic press, 1981.

D. Rouby, S. Raillard, F. Guillocheau, R. Bouroullec, and T. Nalpas. Kinematics of a growth fault/raft system on the West African margin using 3-D restoration. *Journal of Structural Geology*, 24: 783–796, 2002. doi: 10.1016/S0191-8141(01)00108-0.

M. R. Santi, J. L. E. Campos, and L. F. Martha. 3D Geological Restoration using a Finite Element Approach. In *Gocad Proceedings: 23th Gocad Meeting, Association Scientifique pour la Geologie et ses Applications*, 2003.

D. D. Schultz-Ela. Restoration of cross-sections to constrain deformation processes of extensional terranes. *Marine and Petroleum Geology*, 9(4): 372–388, 1992. doi: 10.1016/0264-8172(92)90049-K.

J. Shewchuk. What is a good linear element? Interpolation, conditioning, anisotropy, and quality measures. *11th International Meshing Roundtable*, 73: 115–126, 2002.

H. Si. TetGen, a Delaunay-based quality tetrahedral mesh generator. *ACM Transactions on Mathematical Software (TOMS)*, 41(2): 1–36, 2015a. doi: 10.1145/2629697.

H. Si. TetGen, 2015b. URL `http://wias-berlin.de/software/tetgen/`.

P. Souloumiac, B. Maillot, and Y. M. Leroy. Bias due to side wall friction in sand box experiments. *Journal of Structural Geology*, 35: 90–101, 2012. doi: 10.1016/j.jsg.2011.11.002.

J. M. Stockmeyer and C. A. Guzofski. Interplay Between Extension, Salt and Pre-Existing Structure, Offshore Angola. In *AAPG Annual Convention and Exhibition*, 2014.

J. M. Stockmeyer, J. H. Shaw, L. T. Billingsley, A. Plesch, M. Wales, L. C. Lavin, R. Knox, and L. Finger. in press, Geomechanical restoration as a tool for fractured reservoir characterization: application to the Permian Basin, West Texas. *AAPG Bulletin*, 2017. doi: 10.1306/03231716076.

P. Tang, C. Wang, and X. Dai. A majorized Newton-CG augmented Lagrangian-based finite element method for 3D restoration of geological models. *Computers & Geosciences*, 89: 200–206, 2016. ISSN 0098-3004. doi: 10.1016/j.cageo.2016.01.013.

P. Victor and I. Moretti. Polygonal fault systems and channel boudinage: 3D analysis of multidirectional extension in analogue sandbox experiments. *Marine and Petroleum Geology*, 23(7): 777–789, 2006. doi: 10.1016/j.marpetgeo.2006.06.004.

O. Vidal-Royo, N. Cardozo, J. A. Muñoz, S. Hardy, and L. Maerten. Multiple mechanisms driving detachment folding as deduced from 3D reconstruction and geomechanical restoration: the Pico del Aguila anticline (External Sierras, Southern Pyrenees). *Basin Research*, 24(3): 295–313, 2012. doi: 10.1111/j.1365-2117.2011.00525.x.

O. Vidal-Royo, T. E. Hearon IV, C. D. Connors, S. Bland, F. Schaefer, O. Ferrer, A. Mora, J. de Vera, C. A. Guzofski, F. Rodríguez, E. J.-P. Blanc, and A. P. M. Vaughan. Introduction to special section: Balancing, restoration, and palinspastic reconstruction. *Interpretation*, 3(4): SAAi—-SAAiii, 2015. doi: 10.1190/INT2015-0916-SPSEINTRO.1.

R. Weijermars, M. P. A. Jackson, and B. Vendeville. Rheological and tectonic modeling of salt provinces. *Tectonophysics*, 217(1-2): 143–174, 1993. doi: 10.1016/0040-1951(93)90208-2.

J. F. Wellmann, F. G. Horowitz, E. Schill, and K. Regenauer-Lieb. Towards incorporating uncertainty of structural data in 3D geological inversion. *Tectonophysics*, 490(3): 141–151, 2010. doi: 10.1016/j.tecto.2010.04.022.

G. D. Williams, S. J. Kane, T. S. Buddin, and A. J. Richards. Restoration and balance of complex folded and faulted rock volumes: flexural flattening, jigsaw fitting and decompaction in three dimensions. *Tectonophysics*, 273(3): 203–218, 1997. doi: 10.1016/S0040-1951(96)00282-X.

P. Wriggers and T. A. Laursen. *Computational contact mechanics*. Springer, 2006. ISBN 9783540326083. doi: 10.1007/978-3-540-32609-0.

J. E. Wu, K. McClay, P. Whitehouse, and T. Dooley. 4D analogue modelling of transtensional pull-apart basins. *Marine and Petroleum Geology*, 26(8): 1608–1623, 2009. doi: 10.1016/j.marpetgeo.2008.06.007.

H. Xiao and J. Suppe. Origin of Rollover (1). *AAPG Bulletin*, 76(4): 509–529, 1992.

Y. Yamada and K. McClay. Application of geometric models to inverted listric fault systems in sandbox experiments. Paper 1: 2D hanging wall deformation and section restoration. *Journal of Structural Geology*, 25(9): 1551–1560, 2003. doi: 10.1016/S0191-8141(02)00181-5.

B. Zehner, J. H. Börner, I. Görz, and K. Spitzer. Workflows for generating tetrahedral meshes for finite element simulations on complex geological structures. *Computers & Geosciences*, 79: 105–117, 2015. doi: 10.1016/j.cageo.2015.02.009.

O. C. Zienkiewicz and R. L. Taylor. *The finite element method, volume 1, the basis*. Butterworth-Heinemann, Oxford, United Kingdom, 5th edition, 2000a.

O. C. Zienkiewicz and R. L. Taylor. *The finite element method, volume 2, solid mechanics*. Butterworth-Heinemann, Oxford, United Kingdom, 5th edition, 2000b.